Focal seizures are organized by feedback between neural activity and ion concentration changes

Damiano Gentiletti,[1] Marco de Curtis,[2] Vadym Gnatkovsky,[2,3] and Piotr Suffczynski,[1*]

Author affiliations:

1 Department of Biomedical Physics, Faculty of Physics, University of Warsaw, 02-093 Warsaw, Poland

2 Epilepsy Unit, Fondazione IRCCS Istituto Neurologico *Carlo Besta*, 20133 Milan, Italy

3 Department of Epileptology, University Hospital Bonn, 53127 Bonn, Germany

[*]Corresponding author: suffa@fuw.edu.pl

Abstract

Human and animal EEG data demonstrate that focal seizures start with low-voltage fast activity, evolve into rhythmic burst discharges and are followed by a period of suppressed background activity. This suggests that processes with dynamics in the range of tens of seconds govern focal seizure evolution. We investigate the processes associated with seizure dynamics by complementing the Hodgkin-Huxley mathematical model with the physical laws that dictate ion movement and maintain ionic gradients. We show that the disturbance of K^+ and Cl^- homeostasis by the fast discharge of inhibitory interneurons is sufficient to initiate seizures, which are maintained by positive feedback between ion concentration changes and neuronal activity. Gradual Na^+ accumulation increases the rate of the Na^+/K^+-pump, creating negative feedback which slows down and terminates ictal discharges and contributes to the postictal state. Our results emphasize ionic dynamics as elementary processes behind seizure generation and indicate targets for new therapeutic strategies.

Introduction

Focal seizure patterns recorded with intracranial and intracerebral electrodes in patients submitted to presurgical evaluation often consist of distinct phases (Franaszczuk et al., 1998; Spencer et al., 1992; Velascol et al., 2000). A frequently observed onset pattern in patients with temporal lobe epilepsy (TLE) is characterized by low-voltage fast (LVF) activity in the gamma range (30–80 Hz) (Avoli et al., 2016; de Curtis & Gnatkovsky, 2009; Lagarde et al., 2019; Perucca et al., 2014). LVF seizure onset is followed by the recruitment of irregular spiking behavior which evolves into periodic burst discharges that gradually decrease in frequency and suddenly cease. Seizures are often followed by a period of reduced EEG amplitude known as postictal EEG suppression. The traditional view on epileptic seizures is that they result from an imbalance of synaptic excitation and inhibition (Bradford, 1995; Bragin et al., 2009). It is unclear how this concept may account for the electroencephalographic complexity of TLE seizures and their characteristic progression from one phase to the next. The findings of several studies have not confirmed the role of synaptic interaction in seizure generation or progression. It has been shown that blocking synaptic transmission via a low Ca^{2+} solution led to the development of synchronized seizure-like events (SLE) in hippocampal CA1 slices (Jefferys & Haas, 1982; Yaari et al., 1983) and in the intact hippocampus (Feng & Durand, 2003). Moreover, the synchronized epileptiform activity can be recorded across two hippocampal regions separated by a mechanical lesion, without the involvement of electrochemical synaptic communication (Lian et al., 2001). Finally, in photosensitive baboons, light-induced neocortical seizure discharges were accompanied by depletion of extracellular Ca^{2+} to levels incompatible with the chemical synaptic transmission (Pumain et al., 1985). Additionally, a paradoxical increase in inhibitory cell firing and a decrease in pyramidal cell activity at seizure onset was documented in *in vitro* rodent slices (Derchansky et al., 2008; Fujiwara-Tsukamoto et al., 2007; Lévesque et al., 2016; Lillis et al., 2012; Ziburkus et al., 2006), in the *in vitro* whole guinea pig brain (Gnatkovsky et al., 2008; Uva et al., 2015), and in human and animal *in vivo* recordings (Elahian et al., 2018; Grasse et al., 2013; Miri et al., 2018; Toyoda et al., 2015; Truccolo et al., 2011). The above-mentioned studies suggest that processes at the network level related to changes in synaptic gains cannot be the sole mechanisms that control seizure generation and progression, and that other factors must be involved in the process of ictogenesis.

Although several non-synaptic mechanisms have been proposed to influence abnormal synchronization (Blauwblomme et al., 2014; de Curtis et al., 2018; Jefferys et al., 2012;

Raimondo et al., 2015), the specific mechanisms responsible for seizure induction, evolution and termination remain unclear. Specifically, the relative contribution of raised extracellular potassium (Avoli et al., 1996; Gnatkovsky et al., 2008) vs. increased intracellular chloride leading to depolarizing GABA responses (Alfonsa et al., 2015; Lillis et al., 2012) remains to be established. In the present study, we investigated the possible mechanisms of the LVF seizure pattern using a realistic computational model of the hippocampal network that included activity-dependent ion concentration changes. We based our simulations on the data recorded in the *in vitro* isolated guinea pig brain preparation, because SLE in this model closely resemble human temporal lobe seizures (de Curtis et al., 2006; de Curtis & Gnatkovsky, 2009) and are initiated by enhanced firing of inhibitory interneurons (Gnatkovsky et al., 2008). We used these experimental recordings to guide our *in silico* study due to the availability of data at the network, cellular and ionic levels. A computer model showed that simulated seizures initiated via increased interneuron discharges, evolved, and terminated autonomously due to activity-dependent ion concentration shifts and homeostatic mechanisms that worked continuously to restore physiological transmembrane ion levels. Our modelling results suggest a link between the seizure termination mechanism and postictal suppression state and predict a specific scaling law of inter-bursting intervals observed at the end of seizures, which was validated experimentally.

Results

The model consisted of five cells, four pyramidal neurons (PY) and a fast-spiking inhibitory interneuron (IN), arranged as a chain structure (Fig. 1). The ionic dynamics of K^+, Na^+, Ca^{2+} and Cl^- were incorporated and activity-dependent changes in their concentrations were computed. Concentration changes in each extracellular or intracellular compartment were dependent on several mechanisms such as active and passive membrane currents, inhibitory synaptic GABAa currents, Na^+/K^+-pump, KCC2 cotransporter, glial K^+ buffer, Ca^{2+} pump and buffer, radial diffusion, longitudinal diffusion and volume changes. Additionally, we included impermeant anions (A^-) with concentration dependent volume changes and bicarbonate ions (HCO_3^-) that contributed to GABAa currents.

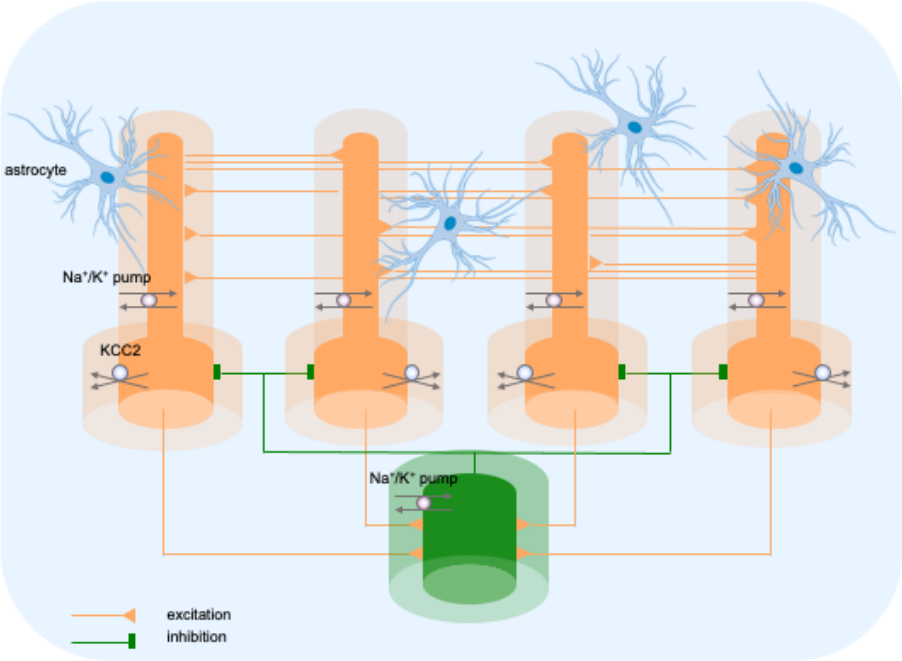

Figure 1. Model diagram. The model consisted of four pyramidal cells (orange) and an interneuron (green) linked by excitatory (AMPA) and inhibitory (GABAa) synaptic connections. Each cellular compartment was surrounded by an interstitial compartment. The interstitial space was enclosed in a common bath (blue) which represented the surrounding tissue and vasculature not included in the model. The model included variable intracellular and extracellular ion concentrations computed according to ionic currents flowing across neuronal membranes, longitudinal diffusion between the dendritic and somatic compartments, radial diffusion between neighboring interstitial compartments and diffusion to/from the bath. Additionally, the model included ionic regulation mechanisms: a Na^+/K^+-pump, a KCC2 cotransporter and K^+ buffering by astrocytes.

Three phases of an LVF onset SLE

Brief perfusions (3 minutes) of 50 microM bicuculline in the isolated guinea pig brain transiently reduces GABAergic inhibition to 60-70% and leads to strong interneuron bursting in the absence of principal cells activity (Gnatkovsky et al., 2008; Uva et al., 2015). Therefore, to initiate a SLE in the model we choose to selectively and transiently enhance discharge of the inhibitory interneuron. In this way we made our model more general and applicable to other experimental data in which paradoxical increase in GABAergic cell firing is observed at seizure onset.

A simulated seizure emerging from normal background activity is shown in Fig. 2. The SLE was triggered by depolarizing current applied to the IN at second 60 (Fig. 2C, yellow trace). Strong firing (initial rate of 150 Hz) of the IN (Fig. 2C) led to small amplitude fast activity in the LFP signal (Fig. 2A between the 60 and 68-second timestamps) associated with the onset of the simulated SLE. After approximately 10 seconds, the PY cells began to generate a strong tonic discharge, resulting in an irregular LFP spiking signal with increased amplitude typically associated with the SLE tonic phase (Fig. 2B; 65–80 seconds). Approximately 20 seconds after the onset of the SLE, the cellular firing pattern of PY cells switched from tonic to bursting discharge, leading to LFP oscillations which corresponded to the bursting phase (Fig. 2A, after 80 seconds). The three types of PY cell activity are shown in an extended time scale in Appendix I – figure 1A. As the SLE progressed, the burst rate gradually decreased and ictal discharges spontaneously terminated. Postictally, the SLE was followed by a period of silence for approximately 90 seconds which was visible in the LFP signal and in the PY and IN traces (Fig. 2A–C). After the postictal depression, the background firing reappeared and gradually returned to a baseline level. The SLE discharges were accompanied by significant changes in the intracellular and extracellular ionic concentrations. At the onset of the seizure, extracellular potassium concentration ($[K^+]_o$) increased sharply in the somatic compartment, remained elevated throughout the SLE and slightly decreased toward the end of the episode (Fig. 2D). Intracellular sodium concentration ($[Na^+]_i$) steadily increased during the bursting phase in both somatic and dendritic compartments and reached a plateau around the offset of the SLE (Fig. 2E). Intracellular chloride concentration ($[Cl^-]_i$) exhibited a gradual increase from the beginning of the SLE and was highest at the end of the paroxysmal firing (Fig. 2F).

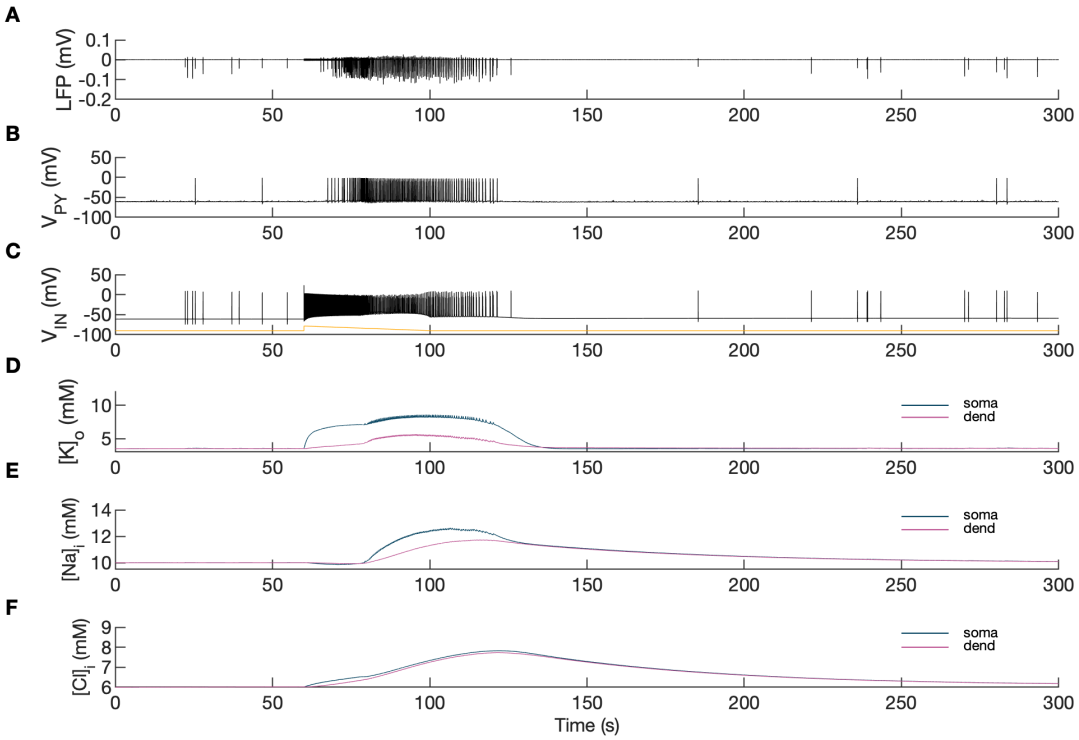

Figure 2. Model behavior during an SLE. (A) Local field potential (LFP) signal. **(B)** Pyramidal cell (PY) membrane potential. **(C)** Interneuron (IN) membrane potential. **(D)** Extracellular potassium concentration. **(E)** Intracellular sodium concentration. **(F)** Intracellular chloride concentration. In the interictal phase (0–60 seconds), the model generated irregular background firing and the ion concentrations were at their resting values (**A–F**). The current injected into the interneuron at second 60 (**C**, yellow) triggered fast IN spiking (**C**, black) which also manifested as low voltage fast activity in the LFP signal (**A**). Approximately 10 seconds after the initiation of the SLE, PY cells initiated tonic firing that subsequently shifted to bursting (**B**). The behavior of the PY cells was reflected in the LFP trace which showed irregular activity and synchronized bursting (**A**). The SLE terminated at approximately second 120 and was followed by a period of reduced excitability (**A–C**). The cellular activity was accompanied by significant ion concentration shifts. Extracellular potassium in the somatic compartment increased sharply and remained elevated throughout the SLE (**D**, dark blue). The $[K^+]_o$ increase in the dendritic compartment was slower and less pronounced (**D**, violet). The intracellular sodium increased gradually toward a plateau (**E**). The intracellular chloride accumulated steadily throughout the SLE (**F**).

A comparison of the simulation results with the available experimental data is shown in Fig. 3. In the isolated guinea pig brain, the SLE activity with an LVF onset pattern (Fig. 3A, top

trace) was induced by 3-min arterial application of bicuculine. The transition from preictal to ictal state which occurred at approximately second 10 was associated with a strong discharge of fast-spiking interneurons (Fig. 3A, third trace) and transient silencing of the PY cells (Fig. 3A, second trace). Within a few seconds from the initiation of the sustained interneuron discharge, the principal PY cells were recruited first into tonic firing and subsequently into bursting discharges which were visible in the PY membrane potential and LFP signals. $[K^+]_o$ sharply increased at the onset of the SLE and remained elevated afterward (Fig. 3A, bottom trace). The *in silico* results (shown for comparison in the same timescale in Fig. 3B) replicated the experimental data in many respects including LFP signal characteristics, cellular firing pattern and $[K^+]_o$ time course.

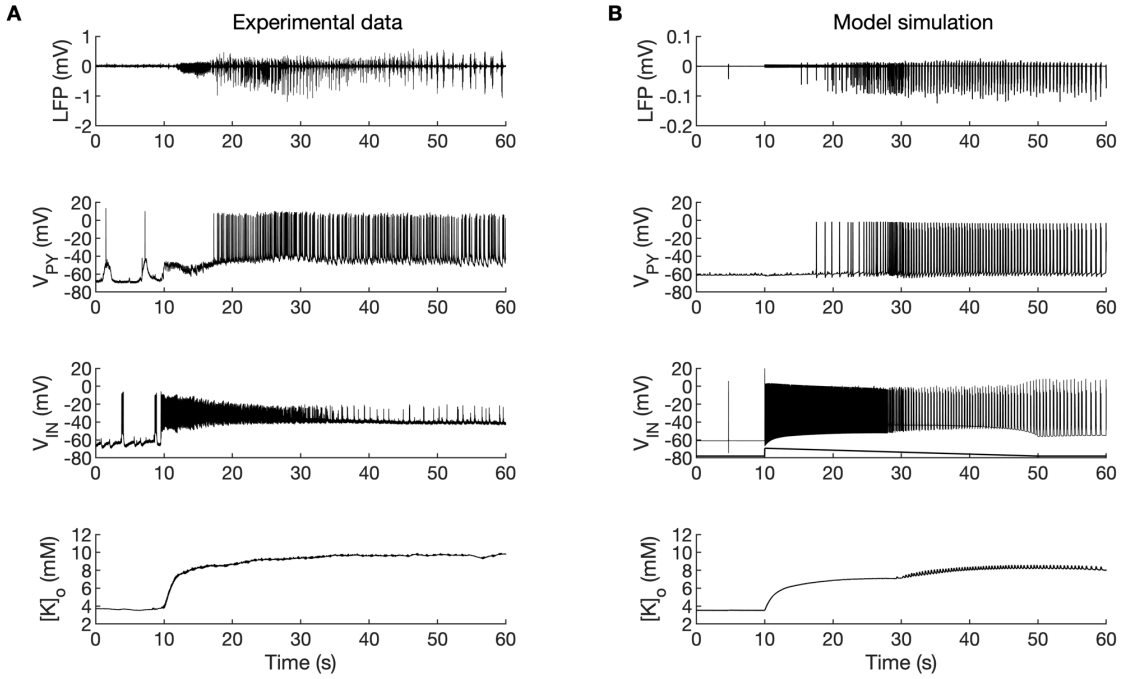

Figure 3. A comparison between the experimental data and the model simulation. (A) Experimental recordings of a seizure-like event (SLE) in the *in vitro* isolated whole guinea pig brain preparation (de Curtis et al., 2006; Gnatkovsky et al., 2008; Uva et al., 2015). From top to bottom: LFP signal, intracellular recording of pyramidal cell (PY) and interneuron (IN), extracellular potassium. The onset of the SLE was associated with increased IN firing, silencing PY and low-voltage fast (LVF) activity in the LFP signal. Approximately 10 seconds after the onset of the SLE, the PY exhibited a tonic and then burst firing behavior. The extracellular potassium increased up to approximately 10 mM at the onset of the SLE and remained elevated

afterward. **(B)** The activity patterns in the LFP signal, pyramidal cells, interneuron and $[K^+]_o$ were reproduced accurately by the model. Signals presented in Fig. 3a were recorded in different experiments. LFP and interneuron data have been published previously (Gentiletti et al., 2017; Gnatkovsky et al., 2008) while pyramidal cell and $[K^+]_o$ data have never been published before.

In the simulations, the excitatory and inhibitory synaptic conductances were "clamped" throughout the entire simulation period, hence, they could not contribute to the progression from one phase to another. Conversely, variations in ion concentrations were expected to affect neuronal excitability. For example, an increase in $[K^+]_o$ reduces the driving force of K^+ currents responsible for hyperpolarized resting membrane potential and spike repolarization. $[Cl^-]_i$ accumulation causes depolarizing shift in E_{GABAa} reducing the efficacy of GABAa inhibition. $[Na^+]_i$ and $[K^+]_o$ affect the rate of the Na^+/K^+-pump that transports three Na^+ ions out of the cell for every two K^+ ions pumped into the cell, thus producing an outward current. Accumulation of $[K^+]_o$ and $[Na^+]_i$ increases the pump rate and enhances the hyperpolarizing pump current. Hence, to determine the intrinsic mechanism that modulates excitability, we first investigated the behavior of the model in response to variations in extracellular potassium and intracellular sodium concentrations and next we considered the role chloride dynamics.

The effects of $[K^+]_o$ and $[Na]_i$ on the network model

Activity-dependent changes in ion concentrations are slow compared to neuronal dynamics, which are relatively fast. To analyze such a system, with slow and fast timescales, it is possible to decouple the fast variables (e.g., membrane potential) from the slow variables (e.g., ionic concentrations). Accordingly, to analyze the role of $[K^+]_o$ and $[Na^+]_i$ in shaping single-cell and network dynamics, we disabled all mechanisms controlling ionic concentrations and analyzed the behavior of the model for different values of $[K^+]_o$ and $[Na^+]_i$. The values of these variables were modified externally and treated as control parameters. To obtain improved affinity with the reference simulation (Fig. 2), the chloride concentration in the somatic and dendritic compartments of the PY cells was set to 7 mM, which corresponded to its mean value during the SLE (Fig. 2F). In the single cell analysis, all synaptic connections were removed. In the network analysis, all synaptic connections were intact except afferent excitatory input, which was removed from PY cells to eliminate the stochastic component from the analysis; depolarizing current injection was removed from the interneuron. The behavior of a single PY cell was analyzed for different values of extracellular potassium in the dendritic ($[K^+]_{o,dend}$) and somatic compartments ($[K^+]_{o,soma}$). During the analysis, for each fixed value of $[K^+]_{o,dend}$, we performed

196 simulations when sweeping the $[K^+]_{o,soma}$ value from 3 mM to 12 mM (in steps of 0.25 mM) in
197 the forward and backward direction. The initial conditions for each $[K^+]_{o,soma}$ value corresponded
198 to the final states in the previous step. For each $[K^+]_{o,soma}$ step, we simulated 5 seconds of activity.
199 After a full sweep with all $[K^+]_{o,soma}$ steps in both directions, the $[K^+]_{o,dend}$ was increased and the
200 analysis was repeated. The analysis was performed for the $[K^+]_{o,dend}$ values in the range of 3–6
201 mM, in steps of 0.5 mM (or 0.25 mM and 0.125 mM if a better resolution was required). We
202 found that the behavior of the single cell and network models was the same for increasing and
203 decreasing steps of $[K^+]_{o,soma}$ with small domains of bistability not larger than one step (0.25
204 mM) between the activity phases. Analysis of the dynamics of a single isolated cell for a
205 reference value of $[Na^+]_i$ at 10 mM can be found in Appendix I – figure 1. In the network analysis,
206 a full sweep with all $[K^+]_{o,soma}$ and $[K^+]_{o,dend}$ steps (as described above) was performed for three
207 different values of $[Na^+]_{i,soma}$ namely, 10 mM, 11 mM and 12 mM. Following Fig. 2E we
208 assumed, that corresponding values of $[Na^+]_{i,dend}$ were lower and were 10 mM, 10.5 mM and 11
209 mM, respectively. The analysis results are shown in Fig. 4A, in which the various activity
210 patterns, i.e., rest, tonic firing and bursting are color-coded (shown on the right). A comparison
211 of the network activities for different values of $[Na^+]_i$ in the three graphs in Fig. 4A demonstrates
212 that the main effect of an increase in $[Na^+]_i$ was a shrinking of the tonic and bursting domains
213 and an expansion of the resting domain due to upregulation of the hyperpolarizing effect of
214 increased $[Na^+]_i$ on the pump current.

215 **The evolution of the SLE mediated by $[K^+]_o$ and $[Na]_i$**

216 In the previous section, the influence of $[K^+]_o$ and $[Na]_i$ on network behavior was examined
217 without accounting for the time factor. Here, we present a fast-slow system analysis approach
218 that considers the time evolution of ionic concentrations, as shown in Fig. 2. Hence, we assessed
219 the dependence of the evolution of an SLE on externally manipulated changes in $[K^+]_o$ and $[Na]_i$
220 with fixed concentrations of all other ions. As in Fig. 4A, the chloride concentration in the
221 somatic and dendritic compartments of the PY cells was set to 7 mM . To schematically describe
222 the extracellular potassium time course from preictal to postictal state (as shown in Fig. 2D), we
223 identified four distinct stages (as shown in Fig. 4B top panel): I) a sharp increase in $[K^+]_{o,soma}$,
224 II) elevated $[K^+]_{o,soma}$, a slow increase in $[K^+]_{o,dend}$, III) a slow decrease in $[K^+]_{o,soma}$ and $[K^+]_{o,dend}$,
225 IV) a decrease in $[K^+]_{o,soma}$ and $[K^+]_{o,dend}$ back to their resting values. Variations in potassium
226 concentrations were accompanied by changes in $[Na^+]_i$ (Fig. 2E). In the preictal period and
227 during the SLE tonic firing phase, $[Na^+]_i$ in the soma and dendrite was stable, while it increased

during the burst firing phase and reached a plateau toward the end of the episode. In the postictal period, $[Na^+]_i$ in both compartments slowly returned to the initial value. The time course of $[Na^+]_i$ approximating intracellular somatic and dendritic sodium evolution is shown in Fig. 4B (middle panel). The corresponding representative PY cell activity is shown in Fig. 4B (bottom trace). To distinguish different SLE phases, the PY cell activity pattern was marked using a color-code, as in Fig. 4A. As $[K^+]_o$ and $[Na^+]_i$ followed their predefined time course, PY cells exhibited transitions from rest to tonic firing, progressed into bursting with a slowing-down pattern and eventually returned to the resting state. In the postictal period (after stage IV), the $[Na^+]_i$ remained elevated for more than 40 seconds (Fig. 4B middle panel) giving rise to an enhanced hyperpolarizing Na^+/K^+-pump current that reduced the excitability of the network and contributed to postictal depression, as described in the last paragraph (Fig. 7). To further observe the time evolution of the SLE in the $[K^+]_{o,soma}$, $[K^+]_{o,dend}$ parameter space, we superimposed potassium changes on the bifurcation diagrams in Fig. 4A. The distinct stages of the potassium time course are marked by arrows. The crossing of a border by an arrow corresponds to a transition between different firing regimes. The initial increase of somatic $[K^+]_o$ (stage I) led to a transition from the resting state to tonic firing (Fig. 4A, first panel), while a subsequent increase of dendritic $[K^+]_o$ (stage II) led to a transition from tonic firing to bursting (Fig. 4A, middle panel). A subsequent decrease in somatic and dendritic $[K^+]_o$ (stage III) led to the termination of the SLE, as the cell activity reentered the resting state region (Fig. 4A, last panel). After termination of the SLE, $[K^+]_{o,soma}$ and $[K^+]_{o,dend}$ returned to their resting values (stage IV in Fig. 4A, last panel).

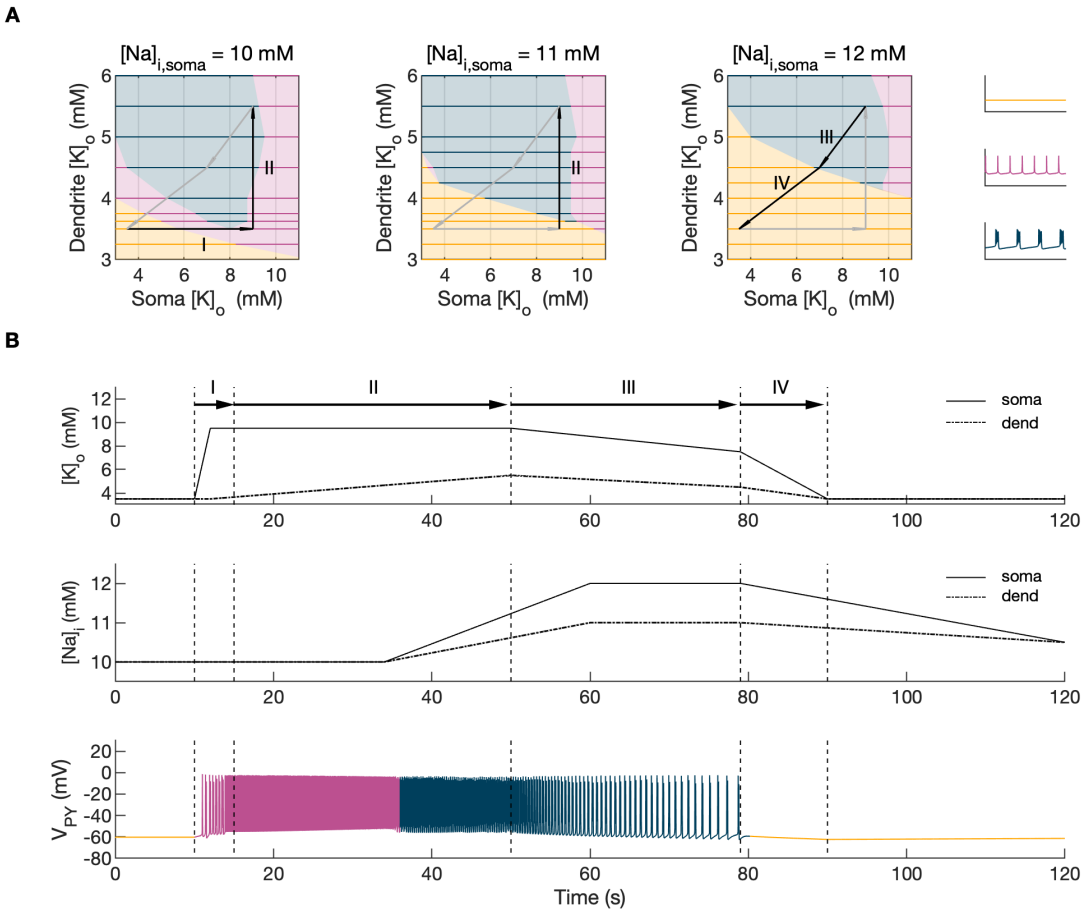

Figure 4. A bifurcation diagram of the model. In the bifurcation analysis extracellular potassium and intracellular sodium concentrations in the PY and IN cells were control parameters. Concentrations of all other ions were fixed at their reference values (except chloride: $[Cl^-]_{i,soma}$, $[Cl^-]_{i,dend}$ equal to 7 mM), all ion accumulation mechanisms were blocked and background input was removed. **(A)** Bifurcation diagrams showing the dependence of the behavior of the model on $[K^+]_{o,dend}$ and $[K^+]_{o,soma}$ for varying values of $[Na^+]_{i,soma}$, $[Na^+]_{i,dend}$. The diagram colors correspond to types of activity shown on the right: rest (yellow), tonic firing (violet) and bursting (dark blue). An increase in $[Na^+]_i$ progressively decreased the domains of tonic firing and bursting and increased the resting domain indicating a general decrease in network excitability. The black and gray arrows correspond to the evolution of $[K^+]_{o,soma}$, $[K^+]_{o,dend}$ during different phases of the SLE, shown in part **B**. **(B)** A simulation of the model with $[K^+]_{o,soma}$, $[K^+]_{o,dend}$ and $[Na^+]_{i,soma}$, $[Na^+]_{i,dend}$ as the external control parameters, that illustrated the occurrence of transitions between different types of activity during the SLE. The top two panels show the time course of $[K^+]_{o,soma}$, $[K^+]_{o,dend}$ and $[Na^+]_{i,soma}$, $[Na^+]_{i,dend}$ and approximate their evolution during the SLE (Fig. 2). The third panel shows the resulting PY cell

265 behavior. The parameter evolution is divided into four phases indicated by the arrows denoted
266 as I–IV in part **A** and **B**. Phase I corresponds to a sharp increase in $[K^+]_{o,soma}$ which led to a
267 transition from rest to tonic firing (marked as a black arrow 'I' in the first panel in **A**). Phase II
268 corresponds to a slow increase in $[K^+]_{o,dend}$ which led to a transition from tonic firing to bursting
269 (marked as a black arrow 'II' in the first and second panels in **A**). Phase III represents a period
270 of increased $[Na^+]_{i,soma}$, $[Na^+]_{i,dend}$ and decreasing $[K^+]_{o,soma}$ and $[K^+]_{o,dend}$ which led to the
271 termination of the SLE (represented by a black arrow 'III' with its tip in the yellow domain in
272 the third panel in **A**). Phase IV corresponds to the postictal period with elevated $[Na^+]_i$ and a
273 return of $[K^+]_{o,soma}$, $[K^+]_{o,dend}$ to their baseline values (marked as a black arrow 'IV' in the third
274 panel in **A**).

275 **The role of $[Cl^-]_i$**

276 Chloride accumulation depends on Cl^- influx through chloride leak and GABAa receptor
277 channels, but it is also affected by variations in potassium concentrations mediated via KCC2
278 cotransport. Hence, chloride and potassium could not be considered as independent control
279 parameters in the fast-slow system analysis approach. Furthermore, visualization of the results
280 with five control parameters ($[K^+]_{o,soma}$, $[K^+]_{o,dend}$, $[Na^+]_{i,soma}$, $[Na^+]_{i,dend}$ and $[Cl^-]_i$) is challenging.
281 Therefore, to evaluate the role of chloride accumulation, we compared the reference model with
282 the model in which chloride dynamics was excluded (Fig. 5). When considering the role of
283 chloride homeostasis mediated via KCC2, the direction of K–Cl cotransport depends on the E_{Cl}
284 vs E_K or the ratio $[K^+]_i[Cl^-]_i/[K^+]_o[Cl^-]_o$ (Payne et al., 2003). If the ratio is greater than 1, KCC2
285 extrudes Cl^- and K^+. If E_K is greater than E_{Cl}, the KCC2 flow is reversed and Cl^- and K^+ ions are
286 transported into the cell. When chloride accumulation was removed (Fig. 5A), the reversal
287 potentials of the Cl^- and GABAa currents (E_{Cl} and E_{GABAa}) were fixed (blue and light blue lines
288 in Fig. 5A, second panel). Under such conditions, the firing of the interneuron (Fig. 5A, third
289 panel) exerted a steady inhibitory influence on the PY cells. Additionally, it increased $[K^+]_o$
290 above fixed $[Cl^-]_i$ level (Fig. 5A, fourth panel). As a result, E_K exceeded E_{Cl} and the KCC2
291 transported K^+ and Cl^- into the cells (Fig. 5A, fifth panel) and reduced the external K^+
292 concentration. All these effects transiently increased the PY cells tonic firing but the bursting
293 SLE phase was not manifested (Fig. 5A, first and second panel). Conversely, activation of the
294 IN in the reference model, with chloride dynamics intact, led to a typical SLE (Fig. 5B, top
295 panel). The $[Cl^-]_i$ accumulation was dominated by Cl^- influx through GABAa receptors and to
296 lesser degree by KCC2 cotransport (Fig 5B, fifth and bottom panel). It led to enhanced

excitability in two ways: i) by increasing the chloride reversal potential (blue line in Fig. 5B, second panel) toward the PY membrane potential, reducing the hyperpolarizing chloride leak current; ii) by increasing the GABAa reversal potential that approached the PY cell membrane potential (Fig. 5B, second panel, light blue), reducing the postsynaptic inhibitory current. These changes led stronger tonic firing of PY cells, which contributed to enhanced $[K^+]_o$ accumulation (Fig. 5B, third panel) leading to the transition into the SLE bursting phase.

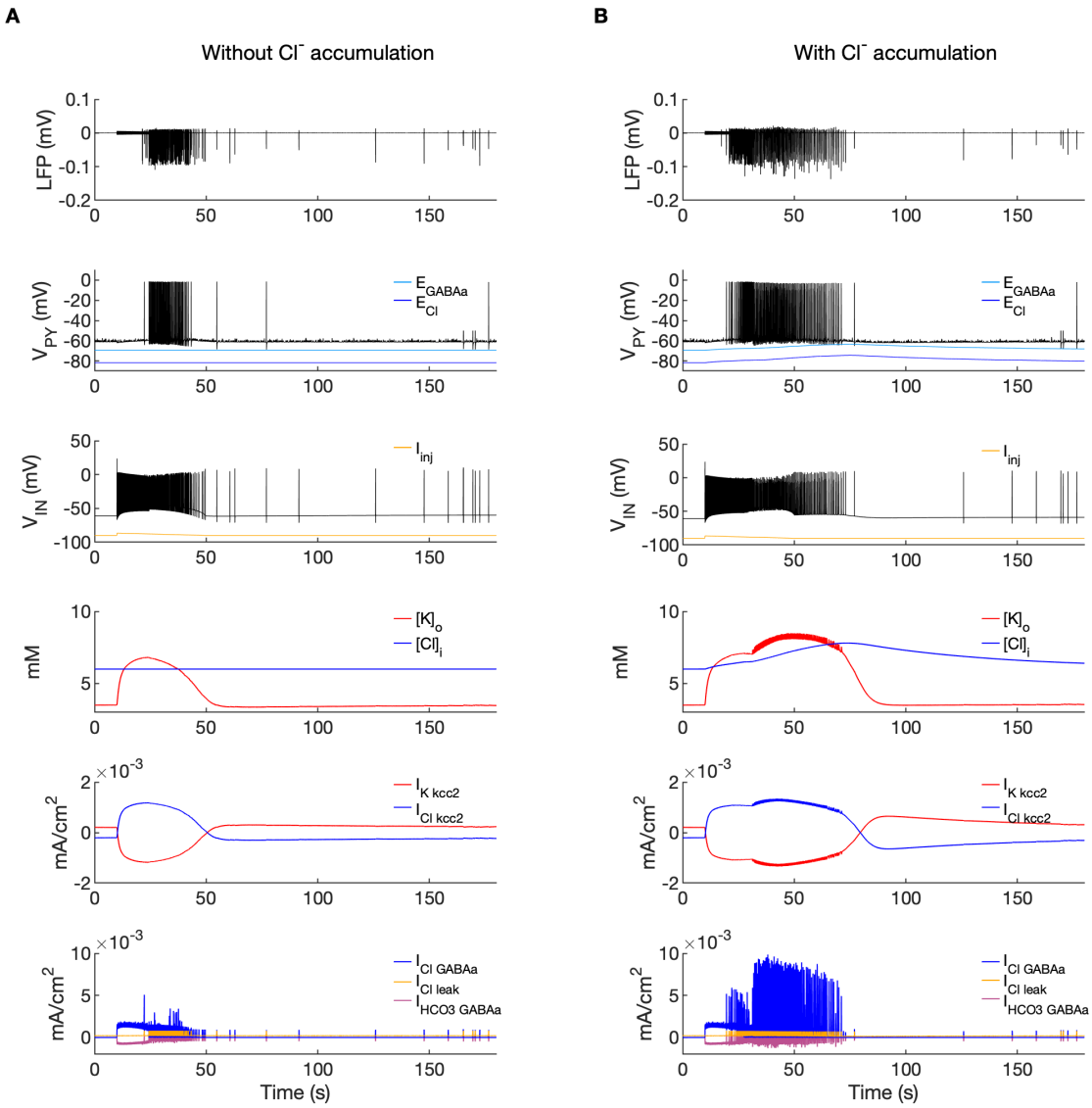

Figure 5. A comparison of the model without and with chloride accumulation. The six panels in each column show respectively (from top to bottom): the LFP signal, the PY cell membrane potential, the IN membrane potential, the extracellular potassium concentration and intracellular chloride concentration, the chloride and potassium KCC2 currents in the somatic

compartments and the GABAa synaptic currents (Cl^- and HCO_3^-) together with the leak chloride current. Additionally, the equilibrium potential of chloride and GABAa are shown in the second panel from the top. **(A)** When the $[Cl^-]_i$ accumulation mechanism was blocked, the chloride concentration was fixed at the reference value (fourth panel, blue). Without chloride accumulation, the PY cell (second panel) fired tonic train of spikes due to transient rise in $[K^+]_o$ (fourth panel, red) mediated by the IN discharge triggered by the current injection (third panel, yellow). Elevated $[K^+]_o$ and fixed $[Cl^-]_i$ promoted K^+ influx via KCC2 (fifth panel, red), thus lowering $[K^+]_o$ and further preventing the generation of the full SLE. **(B)** With chloride accumulation, the IN discharge led to an increase in E_{Cl} and E_{GABAa} (second panel, blue and light blue) which reduced the hyperpolarizing $I_{Cl,leak}$ and I_{GABAa} currents and enhanced excitability. The increase in firing rate of the PY cells led to prolonged $[K^+]_o$ accumulation (fourth panel, red) leading to the full SLE.

Model predictions

The computer model generated predictions about features that were not explicitly implemented but were consequences of the elementary neurobiological mechanisms used to create the model. These phenomena are described below. The experimental confirmation of features predicted by a model is an essential step in model validation.

The evolution of the inter-burst interval duration

It is well known that muscle jerking during the clonic phase of tonic-clonic seizure slows down before ceasing when seizure ends (Bromfield et al., 2006). Frequency slowing has also been observed in video sequences (Kalitzin et al., 2016) and electrographic counterparts of a seizure revealed by either EEG (Franaszczuk et al., 1998; Schiff et al., 2000) or EMG (Conradsen et al., 2013). In the model, a gradual increase in the interval between ictal bursts (IBI) was visible (Fig. 2A and 3B). To observe the evolution of the IBI more precisely and identify the scaling pattern, the background noise was removed from the simulation. The absence of excitatory dendritic synaptic input was compensated with a steady depolarizing DC current of 1.85 pA injected into the dendrites of all PY cells. Current intensity was adjusted to preserve the original duration of the SLE as observed in the model with the background noise present. A simulated SLE trace and the detected ictal bursts (short bars) are shown in Fig. 6A (top panel). The evolution of the IBI is shown below with either a linear (Fig. 6A, middle panel) or a logarithmic (Fig. 6A, bottom panel) y-axis. The IBI on the semi-log graph laid on a straight line suggesting an exponential

relationship. The evolution of the IBI during an SLE in a whole-brain *in vitro* preparation (Fig. 6B) and a human TLE seizure (Fig. 6C) exhibited the same characteristics. An exponential relationship was confirmed via the root mean square error (RMSE) calculated for linear and exponential fits. In all examples, the exponential fit had a lower RMSE.

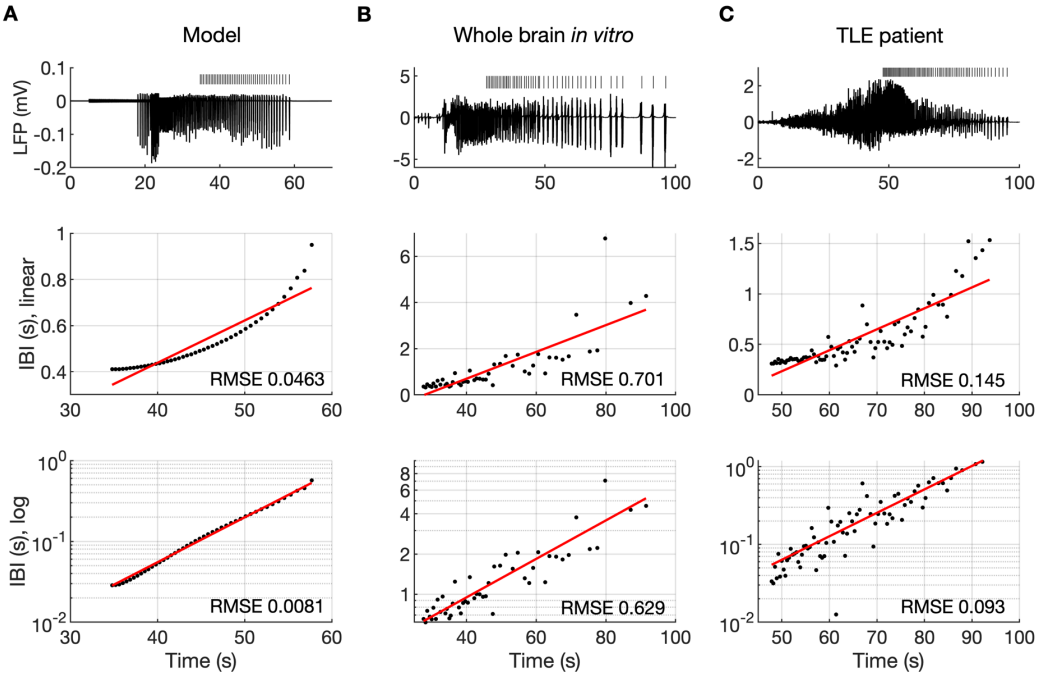

Figure 6. The evolution of IBI in the model and experimental data. (A) In the simulation, the background input was removed and compensated with a small depolarizing current injected into the PY cells to preserve the duration of the SLE. A decreasing rate of bursting is visible in the LPF signal and in the detected bursts marked above the trace (top panel). The evolution of the IBI is shown with the y-axis on a linear scale (middle panel) and a log scale (bottom). On a linear y-axis plot, the data appear curved while on a semi-log plot they lay on a straight line, suggesting exponential scaling of the IBI with time. The red line in each plot represents the best fit for the detected IBI; linear function (middle panel) and exponential function providing a linear relationship on a semi-log plot (bottom panel). The root mean square error (RMSE) between the data points and fitted function is shown in each window. The exponential function fit yielded a smaller RMSE compared to the linear fit, providing quantitative confirmation that at the end of the simulated SLE, the IBI duration increased exponentially, rather than linearly, with time. **(B)** The evolution of the IBI during the SLE induced by application of bicuculline in the whole-brain *in vitro* preparation (Boido et al., 2014; Gnatkovsky et al., 2008). **(C)** IBI evolution during a seizure recorded with intracerebral electrodes positioned in the temporal lobe in a patient

359 submitted to presurgical evaluation (courtesy of Laura Tassi, Epilepsy Surgery Center, Niguarda
360 Hospital, Milano, Italy). In **B** and **C**, the detected IBI lay on a straight line on the semi-log plot
361 and the exponential fit resulted in a smaller RMSE compared to the linear fit, validating the
362 model prediction of an exponential increase in the IBI at the end of a seizure. The linear fit, $IBI(t)$
363 $= A + Bt$, was obtained using the *polyfit* procedure, while the exponential function, $IBI(t) =$
364 $A+Bexp(Ct)$, was fitted using the *fminsearch* procedure in Matlab.

365 *The postictal period*

366 An additional model prediction concerned the postictal period which is characterized by reduced
367 excitability and firing. As shown in Fig. 2A–C, after the termination of an SLE there was an
368 approximate 90-second period during which firing was either absent or reduced with respect to
369 the interictal period. The exact duration of the postictal period was difficult to assess, as the gap
370 in firing after the SLE was dependent on background fluctuations. To directly investigate the
371 network excitability, we analyzed the responsiveness of the model to external periodic
372 stimulation (see Boido et al. (2014)). The background noise was removed and was compensated
373 with a steady depolarizing current, as in Fig. 6. Stimulation was delivered by activating the
374 excitatory synapses every 5 seconds at each PY soma (arrows in Fig. 7B). The amplitude of the
375 excitatory postsynaptic current (EPSC) was set at just above the threshold for triggering the spike
376 in the interictal period (before the timestamp at 60 seconds). The external stimulation triggered
377 a burst and two single spike responses after the SLE termination (Fig. 7, vertical broken line)
378 and failed to trigger a suprathreshold response for approximately 90 seconds afterwards. In line
379 with the PY response pattern, no response to the simulated stimulation was observed in the LFP
380 signal during the postictal suppression period (Fig. 7A). The high excitability immediately after
381 termination of the SLE (timestamps between seconds 110 and 125) was correlated with elevated
382 $[K^+]_o$ which was present shortly after the SLE (Fig. 7C). The subsequent postictal reduction of
383 excitability was associated with decay of $[K^+]_o$ and an increased hyperpolarizing Na^+/K^+-pump
384 current in somatic and dendritic compartments. The pump current decayed with a slower time
385 constant associated with a gradual clearance of $[Na^+]_i$ by the pump (Fig. 7DE).

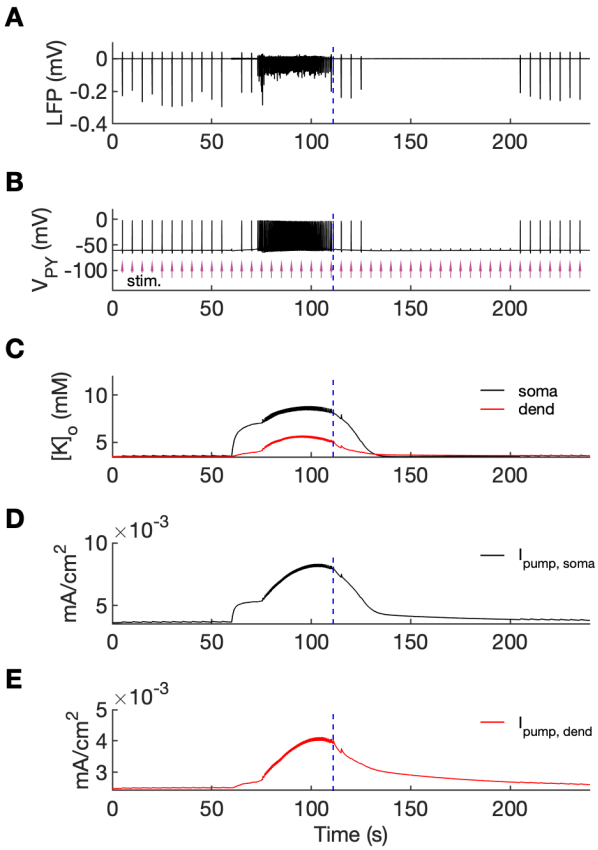

Figure 7. An analysis of network excitability in the postictal period. In this figure, the background input was removed from the simulation and compensated with a small depolarizing current injected into the PY cells, as in Fig. 6. **(A)** The LFP signal. **(B)** The PY cell membrane potential with external periodic stimulation delivered every 5 seconds, marked by the arrows (violet, stim.). The amplitude of the stimulation was set at just above the threshold for triggering a spike in the interictal period. **(C)** The extracellular potassium in the somatic and dendritic compartments. **(D and E)** The net Na^+/K^+-pump current in the somatic and dendritic compartment, respectively. The vertical broken line (blue) in all panels marks the SLE offset time without periodic stimulation. Immediately after termination of the SLE, the network was still excitable due to increased $[K^+]_o$. Shortly afterward, the excitability decreased due to an increased Na^+/K^+-pump current that outlasted the increase in $[K^+]_o$. Increased I_{pump} and decreased $[K^+]_o$ which occurred shortly after the termination of the SLE, led to a postictal period during which the network did not respond to external stimulation for approximately 90 seconds.

Discussion

The present study aimed to better define the mechanisms underlying focal seizures. The ictal pattern most frequently observed in human and experimental TLE, i.e., the LVF onset pattern, exhibits a stereotypical sequence of fast activity, irregular spiking and periodic bursting (as shown in Fig. 3A, first panel) (Avoli et al., 2016; de Curtis & Avoli, 2016; Devinsky et al., 2018; Velascol et al., 2000). We successfully reproduced this pattern in the computer model by transiently increasing the firing of the IN. After this trigger, the simulated SLE phases evolved autonomously. Our study suggests that various seizure phases and transitions from one phase to another are mediated by feedback mechanisms between neuronal activities, ion concentration changes and ion homeostasis processes. The distinct mechanisms that shape the activities at various seizure stages are discussed below.

Seizure initiation

There is increasing evidence showing that seizures with LVF onset are initiated by discharges of fast-spiking GABAergic interneurons (de Curtis & Avoli, 2016; de Curtis & Gnatkovsky, 2009; Devinsky et al., 2018). Increased interneuron discharges and decreased PY activity around the time of seizure onset were first evidenced in *in vitro* and *in vivo* animal models (Gnatkovsky et al., 2008; Grasse et al., 2013; Lévesque et al., 2016; Lopantsev & Avoli, 1998; Miri et al., 2018; Toyoda et al., 2015; Ziburkus et al., 2006). A similar scenario was observed with single-unit recordings performed during intracerebral presurgical monitoring in neocortical and temporal lobe epilepsy patients (Elahian et al., 2018; Truccolo et al., 2011). Causal relationship between increased interneuron firing and ictogenesis may include intracellular chloride accumulation resulting in shift in E_{GABAa} and/or the elevation of $[K^+]_o$, which leads to subsequent depolarization of PY cells and seizure development (Magloire, Mercier, et al., 2019). The hypothesis suggested by Jensen & Yaari (1997) that seizure initiation is related to an elevation in $[K^+]_o$ caused by a strong initial discharge has been tested in computational models with ion concentration changes. In these simulations, seizure-like activity has been induced by DC stimulation of the PY cells alone (Bazhenov et al., 2004; Buchin et al., 2016; Kager et al., 2002), by a brief increase in $[K^+]_o$ (Fröhlich et al., 2006), by stimulation of the IN and PY cells (Ho & Truccolo, 2016) or by varying the extracellular concentration of K^+ and O_2 (Wei, Ullah, & Schiff, 2014). However, as mentioned above, transitions to spontaneous seizures that begin with LFV pattern were not associated with increased excitatory activity, but with increased firing of inhibitory interneurons.

433 Pyramidal cell – interneuron interplay during SLE was first investigated in computational model
434 of Wei, Ullah, Ingram, et al. (2014) which mimicked 4-aminopyridine (4-AP) and decreased
435 magnesium *in vitro* conditions (Ziburkus et al. 2006). They showed that when potassium
436 diffusion rate around the IN was lower than around the PY cell, IN depolarized and increased its
437 activity and eventually entered depolarization block giving way to strong firing of the PY cell
438 during an SLE. The following *in silico* tests on seizure initiation by selective involvement of
439 fast-spiking interneurons were conducted by us (Gentiletti et al., 2017) and others (González et
440 al., 2018). We demonstrated that an increase in interneuron firing triggered a transition to a self-
441 sustained SLE during which both IN and PY cells were active simultaneously. González et al.
442 (2018) showed that interneuron stimulation by current pulses led to the development of an SLE
443 via a gradual increase in $[K^+]_o$ mediated by Cl^- dependent activation of the KCC2 cotransporter.
444 In our present model, the IN was activated by a depolarizing, decreasing current ramp of 40
445 seconds. Initially, the IN discharge led to the silencing of the PY cells, which was correlated
446 with low amplitude fast activity in the LFP signal. The sustained interneuron activity caused a
447 gradual increase in $[Cl^-]_i$ and $[K^+]_o$ in the PY cells. The increase in $[K^+]_o$ produced a positive
448 shift in the K^+ reversal potential which led to a reduction in the K^+ leak current and membrane
449 depolarization. The accumulation of $[Cl^-]_i$ increased the Cl^- reversal potential and decreased the
450 driving force of the Cl^- ions, which led to a reduction in GABAa IPSC and the Cl^- leak current.
451 A depolarization in the E_K, E_{Cl} and E_{GABAa}, and a weakening of the associated hyperpolarizing
452 currents resulted in a gradual depolarization of the PY cells and sustained firing, which was
453 correlated with the tonic SLE phase.

454 To address the role of potassium and chloride accumulation in seizure initiation, we
455 considered the elevation of $[K^+]_o$ and $[Cl^-]_i$ separately. As shown in Fig. 5, a selective increase
456 in $[K^+]_o$ with a fixed concentration of Cl^- did not trigger full SLE. When $[Cl^-]_i$ was increased and
457 the concentration of $[K^+]_{o,i}$ remained fixed at the reference level the PY cells exhibited normal
458 background firing (not shown). This suggests that in our simulation of seizure initiation by IN a
459 change in the concentrations of both $[K^+]_o$ and $[Cl^-]_i$ act in synergy to mediate full SLE. These
460 findings corroborate the results of a study by Alfonsa et al. (2015) which demonstrated that
461 optogenetic chloride loading of PY cells did not trigger ictal events, while the addition of a
462 subictal dose of 4-AP led to full ictal activity. Our results don't contradict *in vitro* experimental
463 observations that elevated $[K^+]_o$ alone is sufficient to induce epileptiform activity (Jensen &
464 Yaari, 1997; Traynelis & Dingledine, 1988). As shown by a bifurcation diagram (Fig. 4A and

465 Appendix I – figure 1) an increase in $[K^+]_o$ may lead to a transition from a silent state to tonic
466 and burst firing.

467 Although in our model chloride accumulation increased E_{GABAa} and lowered synaptic inhibition
468 contributing to full-blown SLE, we didn't observe depolarizing GABA responses as seen in some
469 *in vitro* studies (Cossart et al., 2005; Miles et al., 2012; Ellender et al., 2014). It should be kept
470 in mind that depolarizing GABA responses were found mainly in immature neurons, which have
471 more depolarized Cl^- gradient (Cherubini et al., 1991). Another possible explanation of limited
472 shift in E_{GABAa} in the model may be related to somatic localisation of inhibitory input from the
473 IN. Following observation that activation of parvalbumin-positive (PV) interneurons was
474 implicated in spontaneous seizures (Toyoda et al., 2015) we simulated soma-targeting, PV
475 interneurons but not dendrite-targeting, somatostatin-expressing (SST) interneruons. To see if
476 more pronounced shift in E_{GABAa} could be observed in SST mediated dendritic responses we
477 reduced size of all model compartments to account for distal dendrites. Under these conditions,
478 strong activation of inhibitory interneuron as in Kaila et al. (1997) led to biphasic,
479 hyperpolarizing-depolarizing GABAa response shown in Appendix I – figure 3. These results
480 are in agreement with other studies suggesting that $[Cl^-]_i$ can change rapidly and contribute to
481 depolarizing GABAa responses especially in the structures with low volume to GABAa receptor
482 density ratio (Staley et al., 1995; Staley & Proctor, 1999).
483 The observation that the development of seizures may be related to an increase in $[K^+]_o$
484 beyond the physiological values suggests that the modulation of $[K^+]_o$ by the use of K^+ chelators
485 is a potential strategy for the control of seizures. Moreover, in our previous work, we
486 demonstrated that an artificial potassium buffer, which mimicked the function of astrocytes by
487 balancing neuronal K^+ release, could reduce neuronal excitability and prevent an SLE
488 (Suffczynski et al., 2017).

489 **The mechanisms of $[K^+]_o$ accumulation**

490 A question arises: what causes $[K^+]_o$ accumulation? The buildup of Cl^- inside the PY neurons
491 during interneuron-induced GABA release results in the activation of the KCC2 cotransporter,
492 which extrudes Cl^- and K^+ into the extracellular space. This hypothesis is supported by *in vitro*
493 experiments which showed that activation of GABAa receptors led to an increase in $[K^+]_o$ and
494 cell depolarization, which were eliminated by the KCC2 inhibitor, furosemide (Viitanen et al.,
495 2010). The above-mentioned hypothesis is also consistent with the findings that the application

496 of the KCC2 blockers VU0240551 and bumetanide prevented SLEs during 4-AP application in
497 rat brain slices (Hamidi & Avoli, 2015). However, it is not clear whether the ictal activity is
498 consistently based on K^+ efflux through KCC2. In the pilocarpine model, the enhancement of
499 KCC2 in principal cortical neurons is associated with a reduction in seizure duration (Magloire,
500 Cornford, et al., 2019). Based on these results, the authors suggested that KCC2 activity does
501 not affect seizure initiation, but influences seizure maintenance during a prolonged period of Cl^-
502 accumulation. The antiepileptic role of enhanced KCC2 activity has also been suggested by
503 Moore et al. (2018), who showed that KCC2 potentiation delayed the onset of an SLE after 4-
504 AP application *in vitro* and reduced the severity of kainate-induced seizures *in vivo*. When
505 considering the role of KCC2 in $[K^+]_o$ and $[Cl^-]_i$ accumulation, it is necessary to note that the
506 direction and magnitude of KCC2 transport depend on the concentration gradients of Cl^- and K^+
507 (Kaila et al., 2014). Under normal conditions, when $[K^+]_o$ is sufficiently controlled by
508 homeostatic mechanisms, GABAergic activity leads to the extrusion of Cl^- and K^+ by KCC2.
509 However, an increase in $[K^+]_o$ may reverse the K^+–Cl^- cotransport, thus contributing to $[K^+]_o$
510 buffering rather than accumulation (Payne, 1997; Thompson & Gahwiler, 1989) The activation
511 of IN in our model led to a rapid increase in K^+ in the narrow extracellular interstitial
512 compartments, while intracellular Cl^- accumulation was more gradual (Fig. 2). This generated
513 an influx of K^+ and Cl^- via KCC2 (Fig. 5B), which led to $[K^+]_o$ buffering and $[Cl^-]_i$ accumulation.
514 The exclusion of KCC2 involvement in the increase in $[K^+]_o$ suggests that the primary
515 mechanism of $[K^+]_o$ accumulation in our model was due to other processes, such as the outward
516 K^+ current that repolarizes action potentials in activated IN and PY cells. This observation is
517 consistent with *in vivo* experimental evidence that showed a significant local $[K^+]_o$ rise due to
518 increased spiking activity following electrical stimulation of the cat cerebral cortex (Heinemann
519 & Lux, 1975).

520 It is worth noting that in our model KCC2 resumes extruding Cl^- shortly after SLE
521 termination (Fig. 5B). Accordingly, $[Cl^-]_i$ build up is observed over the whole SLE. Intracellular
522 chloride imaging during SLE induced *in vitro* by Mg^{2+}-free solution showed that $[Cl^-]_i$ started to
523 decline before the end of SLE (Raimondo, 2013), while during SLE induced *in vivo* by 4-AP
524 $[Cl^-]_i$ recovery begun instantly after SLE offset (Sato et al., 2017). These dissimilar observations
525 might be related to distinct firing patterns of inhibitory and excitatory neurons in 4-AP and low
526 Mg^{2+} seizure models (Codadu et al., 2019), which in turn could lead to different Cl^- and K^+ and
527 accumulation patterns.

528 **The tonic-to-bursting transition**

529 Potassium ions released by interneuron discharges initially diffused to the somatic extracellular
530 compartments of the PY cells and contributed to PY soma depolarization and tonic firing, as
531 described above. The initial fast rise of $[K^+]_o$ in somatic compartment and slower rise in dendritic
532 segment (Fig. 2D) was related to localization of inhibitory neuron near the PY soma.
533 Subsequently, K^+ diffusion from the somatic to dendritic compartments promoted regenerative
534 dendritic spikes in PY cells. The dendritic conductance of voltage-gated K^+ currents associated
535 with spiking was about 10% of the somatic conductance (Fransen et al., 2002) hence release of
536 K^+ ions into the dendritic interstitial space was smaller than in somatic compartment maintaining
537 lower dendritic $[K^+]_o$. High $[K^+]_o$ in the soma and moderately increased $[K^+]_o$ in dendrites
538 favored burst firing (Fig. 4A and Appendix I – figure 1) through the reduction of repolarizing
539 K^+ currents, the activation of a Na^+ persistent current, and a shift from spike after-
540 hyperpolarization toward depolarizing after-potentials. Prolonged depolarization led to the
541 activation of slow M-type K^+ conductance (Appendix I – figure 2), which hyperpolarized the PY
542 cells after a series of fast spikes. The bursting mechanism in our model originated from currents
543 used in the original entorhinal cortex cells model (Fransen et al., 2002) and was similar to the
544 mechanism in CA1 neurons (Golomb et al., 2006).

545 We note that in our model a transition from resting to tonic and then to bursting activity
546 in PY cells is not critically dependent on perisomatic inhibition and would be also observed if
547 we simulated dendrite-targeting, SST interneruons. As shown by the bifurcation diagram in Fig.
548 4A (first panel) an increase in either somatic or dendritic $[K^+]_o$ may lead to a transition from rest
549 to tonic spiking and then bursting. It is in agreement with the study showing that optogenetic
550 activation of either PV or SST inhibitory interneurons can trigger SLE (Yekhlef et al., 2015).

551 **Seizure termination**

552 Various mechanisms underlying seizure termination have been suggested (Lado & Moshé, 2008;
553 Zubler et al., 2014), however, researchers have not yet reached a consensus regarding which one
554 plays a dominant role. In our model, the SLE terminated spontaneously. Following the fast-slow
555 analysis approach (Fröhlich et al., 2006) we created a simplified model in which $[K^+]_{o,soma,}$
556 $[K^+]_{o,dend}$ together with $[Na^+]_{i,\ soma}$ and $[Na^+]_{i,\ dend}$ were treated as control parameters. Hence, the
557 influence of neuronal activity on ionic variations was removed and the dependence of network
558 activity on K^+ and Na^+ concentrations was analyzed (Fig. 4A). When the time course of the

concentration changes of these two ions were tuned to reproduce the decrease in $[K^+]_o$ and increased level of $[Na^+]_i$ observed in the late SLE phase, the ictal activity spontaneously terminated (Fig. 4B). This indicates that SLE cessation in the model can be explained by two coincident factors, namely the decrease in $[K^+]_o$ during stable levels of increased $[Na^+]_i$. An increase in $[Na^+]_i$ led to an increased hyperpolarizing Na^+/K^+-pump current, which increased the firing threshold in the neurons. The increased pump activity also contributed to a progressive decrease in $[K^+]_o$. Potassium repolarization currents increased after each burst and eventually prevented the initiation of a new cycle of the oscillation. The idea that negative feedback between $[Na^+]_i$ accumulation and neuronal firing is responsible for seizure termination was first formulated by Jensen & Yaari (1997). Even though it has not been tested experimentally, this hypothesis is consistent with the observation that the inhibition of Na^+/K^+-pump activity occurring during hypoxia prolongs SLE discharges and shortens post-SLE period in hippocampal slices with blocked synaptic transmission (Haas & Jefferys, 1984). It was also observed that a decrease in Na^+ channel conductance via the antiepileptic drug phenytoin, increased the seizure threshold but prolonged the afterdischarges and seizure durations in the rat kindling model of epilepsy (Ebert et al., 1997). In the computational model developed by the Bazhenov team (Krishnan et al., 2015; Krishnan & Bazhenov, 2011) and Chizhov et al. (2018), a progressive increase in $[Na^+]_i$ and activation of the electrogenic Na^+/K^+-pump were identified as the primary factor of SLE termination. The seizure termination mechanism in the above-mentioned studies is similar to the mechanism observed in the present study, even though different specifications of neuronal mechanisms, network characteristics and seizure morphologies were used.

It should be also noted that activation of the Na^+/K^+-pump by $[Na^+]_i$ is not the only proposed mechanism of seizure termination. An alternative mechanism, also linked to an increase in $[Na^+]_i$, is dependent on the Na^+-activated K^+ channels (Igelström, 2013). Moreover, many other mechanisms such as acidosis (Ziemann et al., 2008), the upregulation of inhibitory neurons (Wen et al., 2015), glutamate depletion (Lado & Moshé, 2008), the depolarization block of neurons mediated by K^+ release from astrocytes (Bragin et al., 1997), after-hyperpolarization due to K^+ channels (Timofeev & Steriade, 2004), postburst depression (Boido et al., 2014), increased synchrony (Schindler et al., 2007) and the release of adenosine (During & Spencer, 1992; Uva & de Curtis, 2020) have been suggested to play a role in seizure termination.

The abrupt termination of a seizure across the entire brain requires long-range communication which may involve thalamocortical interactions (Aracri et al., 2018; Evangelista et al., 2015), travelling waves (Martinet et al., 2017; Proix et al., 2018) and ephaptic interactions (Jefferys, 1995; Shivacharan et al., 2019). Multiple neuromodulatory, ionic, synaptic and neuronal components likely cooperate to terminate a seizure. Further insight into these mechanisms may be obtained by their selective blockage (Uva & de Curtis, 2020), the tracking of EEG signal changes as seizure offset approaches (Boido et al., 2014; Saggio et al., 2020) and from analysis of the duration of postictal suppression (Payne et al., 2018).

Frequency Slowing

The approach of seizure termination is often (but not always) accompanied by an increase in the intervals between successive bursts that form the late seizure phase. Saggio et al. (2020) analyzed frequency slowing in human focal onset seizures and estimated that approximately 40% exhibited unequivocal discharge slowing down toward the end. Burst frequency slowing was confirmed in a study on the entorhinal cortex of the isolated brain preparation during bicuculline- and 4AP-induced SLE (Boido et al., 2014). Our model prediction of the exponential increase in the IBI toward the SLE offset (Fig. 6A) was confirmed with experimental data (Fig. 6BC). These findings are also consistent with those of Bauer et al. (2017), which demonstrated that inter-burst intervals in focal epilepsy patients were predominantly described by the exponential scaling law. Conversely, it has been suggested that depending on the bifurcation which leads to seizure termination, the burst oscillation frequency can be constant or decrease according to the logarithmic or square root relationship (Jirsa et al., 2014). The IBI scaling law depends on the slow process leading to seizure termination. In our model, termination of the seizure was related to the slow evolution of ion concentrations which led to a progressive decrease in excitability, primarily via an increased Na^+/K^+-pump rate. The lower the excitability, the more time it took for the burst firing threshold to be reached. Hence, bursts frequency slowing in the model was causally related to variations in ion concentrations. If the time course of the ionic concentrations were different, the evolution of the IBI would also shift. Several alternative explanations for the increasing inter-burst intervals have been proposed. Bauer et al. (2017) included a plasticity parameter that progressively decoupled spatially distributed neural mass units based on the synchrony level. This mechanism accounted for seizure termination, exponential IBI increase and the presence of a transient postictal state. In the model of Liou et al. (2020) the IBI was constant during seizure expansion and only when the spatial propagation of ictal discharge

ceased, the seizure entered the pre-termination stage with a slowing-down trend. An increase in the IBI in this phase was related to the recovery of inhibition and restoration of the Cl^- concentration gradient. These studies indicate that spatial properties related to seizure propagation and synchrony are other factors that may affect the evolution of the IBI.

The postictal period

Seizures are followed by the suppression of physiological rhythms known as postictal EEG suppression (PES) that lasts for seconds or minutes (Pottkämper et al., 2020). Using the stimulation protocol, we investigated the duration of PES in the model. Our results showed that shortly after termination of the SLE, burst responses were still triggered, however, after few seconds, the excitability decreased and remained reduced for approximately 90 seconds (Fig. 7B). This postictal reduction in excitability was associated with subsequent decay of $[K^+]_o$ and an increased hyperpolarizing Na^+/K^+-pump current, which decreased gradually due to slow clearance of $[Na^+]_i$ by the pump (Fig. 7DE). The PES duration in our model is consistent with a typical 'seconds to minutes' timescale although available estimates depend on the PES duration assessment method. In single-unit recordings in epileptic patients with neocortical seizures neuronal spiking was fully suppressed for 5 to 30 seconds after seizure termination (Truccolo et al., 2011). Average duration of postictal suppression based on EEG features in focal seizure patients was estimated at 17 s (Grigorovsky et al., 2020; Table 1), 120 s (D. E. Payne et al., 2018; Table 1) and around 50-100 s (Bauer et al., 2017; Fig. 5). Our *in silico*-derived prediction that postictal 'silence' depends on the hyperpolarizing Na^+/K^+-pump has been previously suggested (Fisher & Schachter, 2000) and simulated (Krishnan et al., 2015; Krishnan & Bazhenov, 2011). However, in these models, postictal state was generated via reduced $[K^+]_o$ to below baseline level, resulting in a negative shift in E_K and membrane hyperpolarization. A below-reference value of $[K^+]_o$ was observed after seizure termination (Heinemann et al., 1977). In our model, the postictal state was mediated by alternative mechanism related to hyperpolarization via electrogenic Na^+/K^+-pump and was not associated with $[K^+]_o$ undershoot, as $[K^+]_o$ decayed to baseline level after the SLE offset (Fig. 7C). This was also observed in several previous studies (Fisher et al., 1976; Futamachi et al., 1974). The findings generated by our computational model suggest that the mechanisms of seizure termination and PES involve ion homeostatic processes activated and sustained by the excessive seizure discharges, eventually leading to the cessation of the seizure and restoration of the normal state.

Methods

Geometry

The cell morphology was based on entorhinal cortex PY cells and an interneuron model (Fransen et al., 2002), further reduced to equivalent cylinder models. The PY consisted of two compartments: a soma with a length of 20 µm and a diameter of 15 µm, and a dendrite with a length of 450 µm and a diameter of 6.88 µm. The interneuron only had a somatic compartment with a length of 20 µm and a diameter of 15 µm. Each compartment was surrounded by its own extracellular space (ECS). The extracellular compartments were embedded in a common bathing medium which represented the surrounding neural tissue and vasculature. The size of the ECS was estimated by the extracellular volume fraction, α defined as the ratio volume of extracellular space/volume of tissue. We used α = 0.131 which corresponded to the CA1 *st. pyramidale* and a K^+ concentration of 3.5 mM (McBain et al., 1990).

Biophysics

The active membrane currents in the PY were the fast Na^+ and K^+ currents (I_{Na} and I_{Kdr}, respectively) in both compartments and were responsible for action potential generation; a persistent Na^+ current, I_{NaP} in the soma; a high-threshold Ca^{2+} current, I_{CaL} in both compartments; a calcium-dependent after-hyperpolarization K^+ current, I_{KAHP} in both compartments; a fast calcium- and voltage-dependent K^+ current, I_{KC} in both compartments; and a noninactivating muscarinic K^+ current, I_{KM} in the soma. The IN included only the I_{Na} and I_{Kdr} currents responsible for spike generation. All the equations for the active currents were initially based on those described by Fransen et al. (2002), however, an additional modification of the parameters described below was required to account for ionic regulation mechanisms. Simulations were performed using the NEURON simulator with a fixed integration step of 0.05 ms.

Passive properties

The reversal potentials were obtained via the Nernst equation:

$$E_X = 2.3\frac{RT}{zF}\log\left(\frac{[X]_o}{[X]_i}\right)$$

where $[X]_i$ and $[X]_o$ are intra- and extracellular concentrations, respectively, of the ions. X = {Na^+, K^+, Ca^{2+}, Cl^-, HCO_3^-}, F is the Faraday constant, R is the gas constant, z is the valence of

682 the ions and T = 273,16 + 32 is the absolute temperature (Gnatkovsky et al., 2008). A leak
683 current, I_{leak}, was present in all compartments of both cells and was a sum of the leak currents of
684 Na^+, K^+ and Cl^-, modelled as:

685 $$I_{i,leak} = g_{i,leak}(V - E_i)$$

686 where $g_{i,leak}$ is the leak current conductance of the ion of interest i = {Na^+, K^+, Cl^-}. The resting
687 membrane potential was -61 mV in the pyramidal cell and in the interneuron. The specific axial
688 resistance in both cells was set to R_a = 100 Ohm*cm and the specific membrane capacitance was
689 set to C_m = 1μF/cm^2, as in Fransen et al. (2002). Based on the R_a and PY cell geometry, the
690 somato-dendritic coupling conductance, g_c, was calculated as 1.5 mS.
691
692 *Active currents*
693 The original equations used time constant units in seconds (s) and voltage units in volts (V), with
694 0 V corresponding to the resting membrane potential. All equations were modified to account
695 for the millivolt (mV) and millisecond (ms) units used in our model and the voltage was shifted
696 by -60 mV to correspond to the membrane potential relative to the extracellular space, which
697 was assumed to be 0 mV. Additional modifications of the parameters were required to account
698 for the ionic regulation mechanisms that were not present in the original model. I_{NaP}: the
699 activation gate exponent was 2 and the inactivation gate time constant, τ_h, was estimated by
700 fitting the activation function form described by Fransen et al. (2002) to the experimental data
701 (Magistretti & Alonso, 1999). I_{Kdr}: the steady-state activation function, n_{inf}, and the activation
702 gate time constant, τ_n, were estimated by empirical fit to the experimental data (Sah et al., 1988).
703 To increase the firing threshold, the activation curve was shifted toward positive potentials by
704 18 mV in the soma and 10 mV in the dendrites. The model generated spontaneous fast spiking
705 otherwise. I_{KAHP}, I_{KC}: these Ca^{2+}-dependent currents were modelled according to the model
706 described by Traub et al. (2003) and were implemented in ModelDB
707 (https://senselab.med.yale.edu/ModelDB/), accession number 20756. Due to the arbitrary units
708 for Ca^{2+} concentration in Traub's model, we modified the current formula to correspond to mM
709 units and resting level of $[Ca^{2+}]_i$ used in our model. In pyramidal cells, the soma and dendrite
710 membrane potentials, V_s and V_d, respectively, were governed by the following Hodgkin-Huxley
711 equations:

712 $$C\frac{dV_s}{dt} = -I_{Na,soma} - I_{NaP} - I_{Kdr,soma} - I_{CaL} - I_{KAHP} - I_{KC} - I_{KM}$$

713 $$- I_{leak} - I_{NaKpump} - I_{Capump} - g_c(V_s - V_d) - I_{syn}$$

$$C\frac{dV_d}{dt} = -I_{Na,dend} - I_{Kdr,dend} - I_{CaL} - I_{KAHP} - I_{KC} - I_{NaKpump} - I_{CaPump} - g_c(V_d - V_s) - I_{syn}$$

Transient sodium current

$$I_{Na,soma} = g_{Na,PYsoma} m^3 h(V - E_{Na})$$

$$I_{Na,dend} = g_{Na,PYdend} m^2 h(V - E_{Na})$$

Persistent sodium current:

$$I_{NaP} = g_{NaP} m^2 h(V - E_{Na})$$

Delayed rectifier:

$$I_{Kdr,soma} = g_{Kdr,PYsoma} n^4 (V - E_K)$$

$$I_{Kdr,dend} = g_{Kdr,PYdend} n^2 (V - E_K)$$

High-threshold Ca^{2+} current:

$$I_{CaL} = g_{CaL} m^2 (V - E_{Ca})$$

Ca^{2+}-dependent K^+ (afterhyperpolarization) current:

$$I_{KAHP} = g_{KAHP} m(V - E_K)$$

Fast Ca^{2+}- and voltage-dependent K^+ current

$$I_{KC} = g_{KC} \min([Ca^{2+}]_i/250,1)\, m(V - E_K)$$

Muscarinic current:

$$I_{KM} = g_{KM} m(V - E_K)$$

Equations of gating variables are given in Table 1. Conductance values are given in Table 2.

Table 1. Gating variables of the ionic currents in pyramidal cell model

Current	Kinetics/time constant (ms)	
$I_{Na,soma}$	$\alpha_m = \frac{0.8(-V-39.8)}{\exp\left(\frac{-V-39.8}{4}\right)-1}$	$\beta_m = \frac{0.7(V+14.8)}{\exp\left(\frac{V+14.8}{5}\right)-1}$
	$\alpha_h = 0.32\exp\left(\frac{-V-15}{18}\right)$	$\beta_h = \frac{10}{\exp\left(\frac{-V-15}{5}\right)+1}$
$I_{Na,dendrite}$	$\alpha_m = \frac{0.32(-V-48.9)}{\exp\left(\frac{-V-48.9}{4}\right)-1}$	$\beta_m = \frac{0.28(V+21.9)}{\exp\left(\frac{V+21.9}{5}\right)-1}$
	$\alpha_h = 0.128\exp\left(\frac{-V-44}{18}\right)$	$\beta_h = \frac{4}{\exp\left(\frac{-V-21}{5}\right)}$

I_{NaP}	$m_\infty = \frac{1}{1+\exp\left(\frac{-48.7-V}{4.4}\right)}$	$\tau_m = \frac{1}{\frac{0.091(V+38)}{1-\exp\left(\frac{-V-38}{5}\right)} - \frac{0.062(V+38)}{1-\exp\left(\frac{V+38}{5}\right)}}$
	$h_\infty = \frac{1}{1+\exp\left(\frac{48.8+V}{9.98}\right)}$	if $V_m \leq -60$: $\tau_m = 3700 + \frac{2000}{\frac{0.091(V+60)}{1-\exp\left(\frac{-V-60}{5}\right)} - \frac{0.062(V+60)}{1-\exp\left(\frac{V+60}{5}\right)}}$ if $V_m > -60$: $\tau_m = 1200 + \frac{8000}{\frac{0.091(V+74)}{1-\exp\left(\frac{-V-74}{5}\right)} - \frac{0.062(V+74)}{1-\exp\left(\frac{V+74}{5}\right)}}$
$I_{Kdr,soma}$	$n_\infty = \frac{1}{1+\exp\left(\frac{-20.8-V}{13.6}\right)}$	$\tau_m = \frac{1.6\left(C+\exp\left(\frac{V}{5}\right)\right)}{D\exp\left(-\frac{V}{40}\right)\left(C+\exp\left(\frac{V}{5}\right)\right)+0.016\exp\left(\frac{V}{5}\right)(64.9+V)}$ $C = -0.00000230599;\ D = 0.0338338$
$I_{Kdr,dend}$	$n_\infty = \frac{1}{1+\exp\left(\frac{-11.8-V}{13.6}\right)}$	$\tau_m = \frac{1.6\left(C+exp\left(\frac{V}{5}\right)\right)}{Dexp\left(-\frac{V}{40}\right)\left(C+exp\left(\frac{V}{5}\right)\right)+0.016\,exp\left(\frac{V}{5}\right)(64.9+V)}$ $C = -0.00000230599;\ D = 0.0338338$
I_{CaL}	$\alpha_m = \frac{1.6}{1+exp(-0.072(V-5))}$	$\beta_m = \frac{0.02(V+8.9)}{exp\left(\frac{V+8.9}{5}\right)-1}$
I_{KAHP}	$\alpha_m = 2000([Ca]_i - [Ca]_{i,rest})$	$\beta_m = 0.01$
I_{KC}, if $V_m \leq -10$	$\alpha_m = \frac{exp\left(\frac{V+50}{11} - \frac{V+53.5}{27}\right)}{18.975}$	$\beta_m = 2exp\left(-\frac{V+53.5}{27}\right) - \alpha_m$
I_{KC}, if $V_m > -10$	$\alpha_m = 2exp\left(-\frac{V+53.5}{27}\right)$	$\beta_m = 0$
I_{KM}	$m_\infty = \frac{1}{1+exp\left(-\frac{V+35}{5}\right)}$	$\tau_m = \frac{1000}{3.3\left[exp\left(\frac{V+35}{40}\right)\right]+\left[exp\left(-\frac{V+35}{20}\right)\right]}$

Membrane potential of the interneuron was governed by the following Hodgkin-Huxley equations:

$$C\frac{dV}{dt} = -I_{Na} - I_{Kdr} - I_{leak} - I_{NaKpump} - I_{syn} - I_{stim}$$

Current equations, kinetics and time constants of these currents were the same as in pyramidal cell soma. To prevent depolarization block of the IN during current stimulation, activation curve of I_{Na} was shifted 3 mV towards more negative potential values, while activation curve of I_{Kdr} was shifted 19 mV towards more negative potential values.

Table2. Conductances used in the model

Current conductance	Description	Values (S/cm^2)
$g_{Na,leak,PYsoma}$	$I_{Na,leak}$ conductance in PY soma	1.5*10^{-5}
$g_{Na,leak,PYdend}$	$I_{Na,leak}$ conductance in PY dendrite	1.1*10^{-5}
$g_{K,leak,PY}$	$I_{K,leak}$ conductance in PY soma and dendrite	3*10^{-5}
$g_{Cl,leak,PY}$	$I_{Cl,leak}$ conductance in PY soma and dendrite	1*10^{-5}
$g_{Na,PYsoma}$	I_{Na} conductance in PY soma	0.014
$g_{Na,PYdend}$	I_{Na} conductance in PY dendrite	0.0014
$g_{Kdr,PYsoma}$	I_{Kdr} conductance in PY soma	0.032
$g_{Kdr,PYdend}$	I_{Kdr} conductance in PY dendrite	0.0032
g_{NaP}	I_{NaP} conductance in PY soma	60*10^{-5}
g_{CaL}	I_{CaL} conductance in PY soma and dendrite	15*10^{-5}
g_{KAHP}	I_{KAHP} conductance in PY soma and dendrite	5*10^{-5}
g_{KC}	I_{KC} conductance in PY soma and dendrite	0.196*1e3
g_{KM}	I_{KM} conductance in PY soma	0.006
$g_{Na,leak,IN}$	$I_{Na,leak}$ conductance in IN	2.9*10^{-5}
$g_{K,leak,IN}$	$I_{K,leak}$ conductance in IN	6*10^{-5}
$g_{Cl,leak,IN}$	$I_{Cl,leak}$ conductance in IN	1*10^{-5}
$g_{Na,IN}$	I_{Na} conductance in IN	0.013
$g_{Kdr,IN}$	I_{Kdr} conductance in IN	0.027

Ionic dynamics

The model included six types of ions (K^+, Na^+, Cl^-, Ca^{2+}, A^- and HCO_3^-) with variable intra- and extracellular concentrations, except for HCO_3^-, which equilibrium is rapidly attained (Theparambil et al., 2020). The evolution of the ion concentrations was based on the following equations:

$$\frac{d[K^+]_i}{dt} = J_K^i + J_{K,longitudinal}^i + J_{K,KCC2}^i + J_{K,Pump}^i + J_{K,vol}^i$$

$$\frac{d[K^+]_o}{dt} = J_K^o + J_{K,radial} + J_{K,longitudinal}^o + J_{K,bath} + J_{K,KCC2}^o + J_{K,Pump}^o + J_{glia} + J_{K,vol}^o$$

$$\frac{d[Na^+]_i}{dt} = J_{Na}^i + J_{Na,longitudinal}^i + J_{Na,Pump}^i + J_{Na,vol}^i$$

$$\frac{d[Na^+]_o}{dt} = J_{Na}^o + J_{Na,radial} + J_{Na,longitudinal}^o + J_{Na,bath} + J_{Na,Pump}^o + J_{Na,vol}^o$$

$$\frac{d[Cl^-]_i}{dt} = J_{Cl}^i + J_{Cl,GABAa}^i + J_{Cl,longitudinal}^i + J_{Cl,KCC2}^i + J_{Cl,vol}^i$$

$$\frac{d[Cl^-]_o}{dt} = J_{Cl}^o + J_{Cl,GABAa}^o + J_{Cl,longitudinal}^o + J_{Cl,bath} + J_{Cl,KCC2}^o + J_{Cl,vol}^o$$

$$\frac{d[Ca^{2+}]_{i,tot}}{dt} = J_{Ca}^i + J_{Ca,longitudinal}^i + J_{CaPump}^i + J_{Ca,vol}^i$$

$$\frac{d[Ca^+]_o}{dt} = J_{Ca}^o + J_{Ca,longitudinal}^o + J_{CaPump}^o + J_{Ca,vol}^o$$

$$\frac{d[A^-]_i}{dt} = J_{A,vol}^i$$

where $[Ca^{2+}]_{i,tot}$ is the total intracellular calcium concentration (see calcium buffer below). All fluxes (mM/ms) are specified below.

Membrane currents

The contribution of transmembrane currents to variations in intra- and extracellular ion concentrations was obtained via the following equations:

$$J_X^i = -\frac{\sum I_X S}{zFV_i}$$

$$J_X^o = \frac{\sum I_X S}{zFV_o}$$

where the sum of I_X is a net membrane current carrying ion X, S is the surface area of the compartment, z is the valence of the ions, F is the Faraday constant and V_i and V_o are the volumes of the intra- and extracellular compartments.

Longitudinal diffusion.

Longitudinal diffusion of K^+, Na^+, Ca^{2+} and Cl^- was implemented between the somatic and dendritic compartments in the intracellular and extracellular space of the same cell. It was described by Fick's first law:

$$J_{X,longitudinal}^{io} = D_x \frac{([X]_{io,a} - [X]_{io})S}{LV_{io}}$$

where D_x is the diffusion coefficient for the ion X, $[X]_{io}$ is the ion concentration in a given intra- or extracellular compartment, $[X]_{oi,a}$ is the ion concentration in the adjacent compartment, S is the cross-sectional area between the compartments, V_{io} is the compartment volume, L is the distance between the centers of the compartments. The diffusion coefficients were (in um^2/ms): $D_{Na} = 1.33$, $D_K = 1.96$, $D_{Ca} = 0.6$, $D_{Cl} = 2.03$ (as in Somjen et al., 2008).

Radial diffusion.

Na^+ and K^+ ions diffused radially between adjacent extracellular compartments modeled as concentric shells around the neurons. The radial exchange of ions between adjacent shells was described by Fick's first law:

$$J_{X,radial} = D_x \frac{\sum([X]_{o,a} - [X]_o)S}{drV}$$

where $[X]_o$ is the ion concentration in a given shell and the sum goes over all adjacent shells having concentrations $[X]_{o,a}$, V is a given shell volume, dr is the distance between the centers of the shells and S is the surface contact area between the shells calculated at 16% of the total outer shell surface. The electrostatic drift of ions was neglected as the ion movement due to the electrical potential gradient in the extracellular space was small compared to the diffusion.

Diffusion to/from the bath

Radial diffusion of K^+, Na^+ and Cl^- between the ECS and the bath was described by Fick's first law:

$$J_{X,bath} = \frac{1}{s} D_x \frac{([X]_{bath} - [X]_o)S}{drV}$$

where D_x is the diffusion coefficient for the ion X, s is the scaling constant, S is the outer surface of the shell, $[X]_{bath}$ is the bath concentration of the ion X, $[X]_o$ is the ion concentration in a given shell, V is the shell volume, dr is the distance between the extracellular space and the bath (assumed to be half of the shell thickness). Flux J_{bath} represents various processes such as diffusion to more distant areas of the brain and cerebrospinal fluid, active transport of potassium into capillaries and potassium spatial buffering by astrocytes. The effective time constant of these joint processes is likely to be much slower than that of radial and longitudinal diffusion and is described by the scaling constant $s = 4.4*10^4$.

The Na^+/K^+ pump

The Na^+/K^+ pump was modelled as the sodium and potassium transmembrane currents (Kager et al., 2000):

$$I_{Na,Pump} = 3I_{max}flux([Na^+]_i, [K^+]_o)$$

$$I_{K,Pump} = -2I_{max}flux([Na^+]_i, [K^+]_o)$$

$$flux([Na^+]_i, [K^+]_o) = \left(1 + \frac{Km_K}{[K^+]_o}\right)^{-2} \left(1 + \frac{Km_{Na}}{[Na^+]_i}\right)^{-3}$$

with $Km_K = 2$ mM and $Km_{Na} = 10$ mM. I_{max} values were computed for each cell and compartment to balance Na^+ and K^+ membrane currents at rest and were as follows (in mA/cm^2): 0.014 (PY soma), 0.009 (PY dendrite), 0.025 (IN).

KCC2 cotransport

The KCC2 cotransporter currents were modelled according to Wei et al. (2014):

$$I_{K,KCC2} = U_{KCC2} \log\left(\frac{[K^+]_i[Cl^-]_i}{[K^+]_o[Cl^-]_o}\right)$$

$$I_{Cl,KCC2} = -I_{K,KCC2}$$

with cotransporter strength adjusted to balance chloride leak current at rest, U_{KCC2} = 0.002 mA/cm^2.

Glial uptake

Potassium uptake by the glia was modelled as a set of differential equations (Kager et al., 2000):

$$J_{glia} = -k_2[K^+]_o[B] + k_1[KB]$$

$$\frac{d[B]}{dt} = -k_2[K^+]_o[B] + k_1[KB]$$

$$\frac{d[KB]}{dt} = k_2[K^+]_o[B] - k_1[KB]$$

where *[B]* is the free buffer, *[KB]* is the bound buffer (= $[B]_{max}-[B]$), B_{max} = 1100 mM. k_1 = 0.0008 ms^{-1} and $k_2 = \frac{k_1}{1+\exp\left(\frac{[K]_o-16}{-1.25}\right)}$ are backward and forward rate constants, respectively.

The calcium pump and buffer

The calcium pump and buffer which altered the intracellular Ca^{2+} were modelled according to the model implementation of Somjen et al. (2008) in ModelDB, accession number 113446. The calcium pump which extruded Ca^{2+} from the cells was modelled as a Ca^{2+} transmembrane current:

$$I_{CaPump} = \frac{I_{max}}{1 + \frac{K_{pump}}{[Ca^{2+}]_i}}$$

with I_{max} = 2.55 mA/cm^2 and K_{pump} = 0.0069 mM. Intracellular Ca^{2+} was buffered by first-order chemical Ca^{2+} buffer with a total concentration of $[B]_i$ and an equilibrium constant of K_d. Calcium buffering was fast and under the assumption of equilibrium conditions, the relationship between the total and free intracellular calcium concentrations, $[Ca^{2+}]_{i,tot}$ and $[Ca^{2+}]_i$, was given by (Borgdorff, 2002, pg. 27):

$$[Ca^{2+}]_{i,tot} = [Ca^{2+}]_i \frac{[B]_i + K_d + [Ca^{2+}]_i}{K_d + [Ca^{2+}]_i}$$

where $[B]_i$ = 1.562 mM*(V_i^0/V_i), V_i is the intracellular compartment volume, V_i^0 is the intracellular compartment volume at rest and K_d = 0.008 mM.

Volume changes

Volume changes were modelled according to Somjen et al. (2008). The rates of intra- and extracellular volume changes were proportional to the difference in osmotic pressure between the intra- and extracellular compartments and fulfilled the conservation of total volume.

$$\frac{dV_i}{dt} = \Delta$$

$$\frac{dV_o}{dt} = -\Delta$$

where

$$\Delta = \frac{c(\pi_i - \pi_o)}{\tau}$$

$$\pi_i = [Na^+]_i + [K^+]_i + [Cl^-]_i + [Ca^{2+}]_i + [HCO_3^-]_i + [A^-]_i$$

$$\pi_o = [Na^+]_o + [K^+]_o + [Cl^-]_o + [Ca^{2+}]_o + [HCO_3^-]_o + [A^-]_o$$

V_i and V_o are the volumes of the intra- and extracellular compartments and τ = 250 ms. The constant c is introduced for unit conversion and is equal to 1 um^3/mM, hence units of Δ are um^3/ms. The extracellular volume was initially 13.1% of the cellular volume and was allowed to shrink maximally down to 4%. Volume changes affected concentrations but not the total mass of each ion within a compartment. The conservation of mass required additional fluxes:

Intracellular

$$J^i_{X,vol} = -\frac{\Delta}{V_i}[X]_i$$

Extracellular

$$J^{o}_{X,vol} = \frac{\Delta}{V_o}[X]_o$$

Extracellular space (ES) volume shrinks maximally by about 27%, comparable to average reduction of 30% during self-sustained epileptiform discharges (Dietzel et al., 1980). Intracellular space (IS) volume expands about 4%, being a consequence of constant total volume (ES+IS = const). Volume changes and resulting shifts in representative ion concentrations are shown in Appendix I – figure 4. We note that volume changes in our model didn't have big impact on the observed model dynamics. Shifts in ionic gradients contributed by slow volume changes were efficiently compensated by other homeostatic mechanisms, which acted on a faster time scale. In the real tissue astrocyte swelling may be significant and may reduce flow of ions and oxygen (affecting Na^+/K^+-pump activity) contributing to seizures and spreading depression (Hübel & Ullah, 2016). In our model glial cell swelling was not included and its effects on diffusion and the Na^+/K^+-pump were not simulated which is one of the model limitations.

Initial ion concentrations

The initial concentrations were based on existing literature: $[Na^+]_i$, $[Ca^{2+}]_i$, $[Na^+]_o$, $[K^+]_o$, $[Ca^{2+}]_o$ and $[A^-]_o$ (Somjen et al., 2008); $[Cl^-]_i$, $[HCO_3^-]_i$, $[HCO_3^-]_o$ (Doyon et al., 2011); $[K^+]_i$ $[Cl^-]_o$ (Payne et al., 2003). In setting chloride and potassium concentrations we additionally aimed to fulfill $E_K < E_{Cl}$ and $E_{GABAa} \sim -70$ mV (Andersen et al., 1980). The $[A^-]_i$ concentration was set to fulfill osmotic equilibrium condition. Hence, the initial concentrations were as follows (in mM): $[Na^+]_i = 10$, $[Na^+]_o = 140$, $[K^+]_i = 87$, $[K^+]_o = 3.5$, $[Cl^-]_o = 135$, $[Cl^-]_i = 6$, $[Ca^{2+}]_i = 5e\text{-}5$, $[Ca^{2+}]_o = 2$, $[A^-]_i = 187.5$, $[A^-]_o = 0$, $[HCO_3^-]_i = 15$, $[HCO_3^-]_o = 25$. These values gave the following Nernst potentials (in mV): $E_{Na} = 69.4$, $E_K = -84.5$, $E_{Cl} = -81.8$, $E_{Ca} = 139.3$, $E_{HCO3} = -13.4$, $E_{GABAa} = -69.5$.

Resting state

Steady-state conditions at rest were characterized by no net flux of the ions at resting potential (-61 mV). These conditions were determined separately for each cell and compartment. For chloride, KCC2 cotransport strength U_{KCC2} was adjusted to balance Cl^- leak current at rest, i.e.,:

$$I_{Cl,leak} = -I_{Cl,KCC2}$$

For sodium and potassium, first, Na^+ leak current conductance $g_{Na,leak}$ was adjusted to ensure that at rest all passive and voltage-gated membrane currents I_{Na} and I_K are in the ratio -3/2, i.e.,:

$$I_{Na} = -\frac{3}{2}I_K$$

Next, the Na^+/K^+-pump strength I_{max} was adjusted such that I_{Na} and I_K currents were balanced by equal and opposite pump currents:

$$-I_{Na} = I_{Na,pump}$$

$$-I_K = I_{K,Pump}$$

Synaptic connections and model inputs

The pyramidal cells created excitatory AMPA synaptic connections with the interneuron and all other pyramidal cells. The interneuron created an inhibitory $GABA_a$ synaptic connection with each pyramidal cell. Excitatory synapses were placed in the middle of the PY dendrite and the middle of the IN soma. Inhibitory synapses were placed in the middle of the PY soma. The time course of synaptic conductance was modelled with a built-in NEURON mechanism Exp2Syn, implementing a dual exponential function:

$$g = g_{max}\left[\exp\left(-\frac{t}{\tau_2}\right) - \exp\left(-\frac{t}{\tau_1}\right)\right]$$

where the rise and decay time constants, τ_1 and τ_2, were 2 ms and 6 ms, respectively, for all synapses. g_{max} = weight*factor, where the factor was defined so that the normalized peak was 1. The weights for the synapses between the PY and from the PY to the IN were w_{ee} = 0.0002 µS and w_{ei} = 0.0017 µS, respectively. The inhibitory synaptic weight, w_{ie}, was 0.0005 µS. All pyramidal cells received background input modelled as a Poisson spike train, which was different in each cell, activated an excitatory synapse at a rate of 5 Hz and had a synaptic weight w_{input} = 0.0004 µS. To initiate the SLE, a depolarizing ramp current, I_{inj}, was injected into the interneuron, with the initial amplitude of 0.35 nA linearly decreasing toward 0 over 40 seconds. The inhibitory $GABA_a$ postsynaptic currents were carried by Cl^- and HCO_3^- ions (Jedlicka et al., 2010):

$$I_{GABAa} = I_{Cl\,GABAa} + I_{HCO3\,GABAa}$$

$$I_{Cl\,GABAa} = (1-P)g(V - E_{Cl})$$

$$I_{HCO3\,GABAa} = Pg(V - E_{HCO3})$$

$$E_{GABAa} = (1-P)E_{Cl} + PE_{HCO3}$$

where, relative permeability P was 0.18.

Calculation of the LFP

The local field potentials were calculated based on all transmembrane currents in all cells using the following equation (Nunez & Srinivasan, 2006):

$$\phi(r,t) = \frac{1}{4\pi\sigma}\sum_{n=1}^{N}\frac{I_n(t)}{|r - r_n|}$$

Where I_n is a point current source at position r_n (taken as the position of a mid-point of a compartment) and r is the position of the electrode. $\sigma =$ 0.3 S/m is the extracellular conductivity (Lindén et al., 2014). The electrode was located in the middle of the somatic layer of the PY and IN cells, approximately 16 um from the centers of the somas of two neighbouring PY cells. The currents from the interneuron were taken with a weight of 0.2 to decrease their contribution. Also, the influence of the injected current on the LFP was removed. The amplitude of the simulated LFP signal was an order of magnitude smaller than the experimental data. This was due to current point-source approximation and the small number of cells in the modeled network.

Software Accessibility

If accepted, the model will be publicly available in the ModelDB (https://senselab.med.yale.edu/modeldb/)

Acknowledgements

We are grateful to Laura Uva and Laura Librizzi for helpful discussions throughout the preparation of this work and for providing the SLE data from the *in vitro* isolated whole guinea pig brain. We thank Laura Tassi from the *Claudio Munari* Epilepsy Surgery Center of the Niguarda Hospital in Milano, Italy, for providing the intracerebral data on human seizures. The work of MdC and VG was supported by the EPICARE grant of the Associazione Paolo Zorzi for the Neuroscience.

Competing interests

The authors report no competing interests.

References

Alfonsa, H., Merricks, E. M., Codadu, N. K., Cunningham, M. O., Deisseroth, K., Racca, C., & Trevelyan, A. J. (2015). The Contribution of Raised Intraneuronal Chloride to Epileptic Network Activity. *Journal of Neuroscience*, *35*(20), 7715–7726. https://doi.org/10.1523/JNEUROSCI.4105-14.2015

Andersen, P., Dingledine, R., Gjerstad, L., Langmoen, I. A., & Laursen, A. M. (1980). Two different responses of hippocampal pyramidal cells to application of gamma-amino butyric acid. *The Journal of Physiology*, *305*(1), 279–296. https://doi.org/10.1113/jphysiol.1980.sp013363

Aracri, P., de Curtis, M., Forcaia, G., & Uva, L. (2018). Enhanced thalamo-hippocampal synchronization during focal limbic seizures. *Epilepsia*, *59*(9), 1774–1784. https://doi.org/10.1111/epi.14521

Avoli, M., Barbarosie, M., Lücke, A., Nagao, T., Lopantsev, V., & Köhling, R. (1996). Synchronous GABA-Mediated Potentials and Epileptiform Discharges in the Rat Limbic System In Vitro. *The Journal of Neuroscience*, *16*(12), 3912–3924. https://doi.org/10.1523/JNEUROSCI.16-12-03912.1996

Avoli, M., De Curtis, M., Gnatkovsky, V., Gotman, J., Köhling, R., Lévesque, M., Manseau, F., Shiri, Z., & Williams, S. (2016). Specific imbalance of excitatory/inhibitory signaling establishes seizure onset pattern in temporal lobe epilepsy. *Journal of Neurophysiology*, *115*(6), 3229–3237. https://doi.org/10.1152/jn.01128.2015

Bauer, P. R., Thijs, R. D., Lamberts, R. J., Velis, D. N., Visser, G. H., Tolner, E. A., Sander, J. W., Lopes da Silva, F. H., & Kalitzin, S. N. (2017). Dynamics of convulsive seizure termination and postictal generalized EEG suppression. *Brain*, *140*(3), 655–668. https://doi.org/10.1093/brain/aww322

Bazhenov, M., Timofeev, I., Steriade, M., & Sejnowski, T. J. (2004). Potassium model for slow (2-3 Hz) in vivo neocortical paroxysmal oscillations. *Journal of Neurophysiology*, *92*(2), 1116–1132. https://doi.org/10.1152/jn.00529.2003

Blauwblomme, T., Jiruska, P., & Huberfeld, G. (2014). Mechanisms of ictogenesis. In *International Review of Neurobiology* (Vol. 114, pp. 155–185). Academic Press Inc. https://doi.org/10.1016/B978-0-12-418693-4.00007-8

Boido, D., Gnatkovsky, V., Uva, L., Francione, S., & De Curtis, M. (2014). Simultaneous enhancement of excitation and postburst inhibition at the end of focal seizures. *Annals of Neurology*, *76*(6), 826–836. https://doi.org/10.1002/ana.24193

Borgdorff, J. A. (2002). *Calcium dynamics in hippocampal neurones* [University of Amsterdam]. https://hdl.handle.net/11245/1.201021

Bradford, H. F. (1995). Glutamate, GABA and epilepsy. *Progress in Neurobiology*, *47*(6), 477–511. https://doi.org/10.1016/0301-0082(95)00030-5

Bragin, A., Azizyan, A., Almajano, J., & Engel, J. (2009). The Cause of the Imbalance in the Neuronal Network Leading to Seizure Activity Can Be Predicted by the Electrographic Pattern of the Seizure Onset. *Journal of Neuroscience*, *29*(11), 3660–3671. https://doi.org/10.1523/JNEUROSCI.5309-08.2009

Bragin, Anatol, Penttonen, M., & Buzsáki, G. (1997). Termination of Epileptic Afterdischarge in the Hippocampus. *The Journal of Neuroscience*, *17*(7), 2567–2579. https://doi.org/10.1523/JNEUROSCI.17-07-02567.1997

Bromfield, E. B., Cavazos, J. E., & Sirven, J. I. (Eds.). (2006). *An Introduction to Epilepsy [Internet]*. West Hartford (CT): American Epilepsy Society. https://www.ncbi.nlm.nih.gov/books/NBK2508/

Buchin, A., Chizhov, A., Huberfeld, G., Miles, R., & Gutkin, B. S. (2016). Reduced efficacy of the KCC2 cotransporter promotes epileptic oscillations in a subiculum network model. *Journal of Neuroscience*, *36*(46), 11619–11633. https://doi.org/10.1523/JNEUROSCI.4228-15.2016

Cherubini, E., Gaiarsa, J. L., & Ben-Ari, Y. (1991). GABA: an excitatory transmitter in early postnatal life. *Trends in Neurosciences*, *14*(12), 515–519. https://doi.org/10.1016/0166-2236(91)90003-D

Chizhov, A. V., Zefirov, A. V., Amakhin, D. V., Smirnova, E. Y., & Zaitsev, A. V. (2018). Minimal model of interictal and ictal discharges “Epileptor-2.” *PLoS Computational Biology*, *14*(5), 1–25. https://doi.org/10.1371/journal.pcbi.1006186

Codadu, N. K., Graham, R. T., Burman, R. J., Jackson-Taylor, R. T., Raimondo, J. V., Trevelyan, A. J., & Parrish, R. R. (2019). Divergent paths to seizure-like events. *Physiological Reports*, *7*(19). https://doi.org/10.14814/phy2.14226

1011 Conradsen, I., Moldovan, M., Jennum, P., Wolf, P., Farina, D., & Beniczky, S. (2013).
1012 Dynamics of muscle activation during tonic–clonic seizures. *Epilepsy Research*, *104*(1–
1013 2), 84–93. https://doi.org/10.1016/j.eplepsyres.2012.09.004

1014 Cossart, R., Bernard, C., & Ben-Ari, Y. (2005). Multiple facets of GABAergic neurons and
1015 synapses: multiple fates of GABA signalling in epilepsies. *Trends in Neurosciences*,
1016 *28*(2), 108–115. https://doi.org/10.1016/j.tins.2004.11.011

1017 de Curtis, M., & Avoli, M. (2016). GABAergic networks jump-start focal seizures. *Epilepsia*,
1018 *57*(5), 679–687. https://doi.org/10.1111/epi.13370

1019 de Curtis, M., & Gnatkovsky, V. (2009). Reevaluating the mechanisms of focal ictogenesis:
1020 The role of low-voltage fast activity. *Epilepsia*, *50*(12), 2514–2525.
1021 https://doi.org/10.1111/j.1528-1167.2009.02249.x

1022 de Curtis, M., Librizzi, L., & Uva, L. (2006). In Vitro Isolated Guinea Pig Brain. In A.
1023 Pitkänen, P. A. Schwartzkroin, & S. L. Moshé (Eds.), *Models of Seizures and Epilepsy*
1024 (pp. 103–109). Academic Press Inc. https://doi.org/10.1016/B978-012088554-1/50011-6

1025 de Curtis, M., Uva, L., Gnatkovsky, V., & Librizzi, L. (2018). Potassium dynamics and
1026 seizures: Why is potassium ictogenic? *Epilepsy Research*, *143*(April), 50–59.
1027 https://doi.org/10.1016/j.eplepsyres.2018.04.005

1028 Derchansky, M., Jahromi, S. S., Mamani, M., Shin, D. S., Sik, A., & Carlen, P. L. (2008).
1029 Transition to seizures in the isolated immature mouse hippocampus: a switch from
1030 dominant phasic inhibition to dominant phasic excitation. *The Journal of Physiology*,
1031 *586*(2), 477–494. https://doi.org/10.1113/jphysiol.2007.143065

1032 Devinsky, O., Vezzani, A., O'Brien, T. J., Jette, N., Scheffer, I. E., de Curtis, M., & Perucca, P.
1033 (2018). Epilepsy. *Nature Reviews Disease Primers*, *4*(1), 18024.
1034 https://doi.org/10.1038/nrdp.2018.24

1035 Dietzel, I., Heinemann, U., Hofmeier, G., & Lux, H. D. (1980). Transient changes in the size of
1036 the extracellular space in the sensorimotor cortex of cats in relation to stimulus-induced
1037 changes in potassium concentration. *Experimental Brain Research*, *40*(4).
1038 https://doi.org/10.1007/BF00236151

Doyon, N., Prescott, S. A., Castonguay, A., Godin, A. G., Kröger, H., & De Koninck, Y. (2011). Efficacy of Synaptic Inhibition Depends on Multiple, Dynamically Interacting Mechanisms Implicated in Chloride Homeostasis. *PLoS Computational Biology*, *7*(9), e1002149. https://doi.org/10.1371/journal.pcbi.1002149

During, M. J., & Spencer, D. D. (1992). Adenosine: A potential mediator of seizure arrest and postictal refractoriness. *Annals of Neurology*, *32*(5), 618–624. https://doi.org/10.1002/ana.410320504

Ebert, U., Cramer, S., & Löscher, W. (1997). Phenytoin's effect on the spread of seizure activity in the amygdala kindling model. *Naunyn-Schmiedeberg's Archives of Pharmacology*, *356*(3), 341–347. https://doi.org/10.1007/PL00005060

Elahian, B., Lado, N. E., Mankin, E., Vangala, S., Misra, A., Moxon, K., Fried, I., Sharan, A., Yeasin, M., Staba, R., Bragin, A., Avoli, M., Sperling, M. R., Engel, J., & Weiss, S. A. (2018). Low-voltage fast seizures in humans begin with increased interneuron firing. *Annals of Neurology*, *84*(4), 588–600. https://doi.org/10.1002/ana.25325

Ellender, T. J., Raimondo, J. V., Irkle, A., Lamsa, K. P., & Akerman, C. J. (2014). Excitatory effects of parvalbumin-expressing interneurons maintain hippocampal epileptiform activity via synchronous afterdischarges. *Journal of Neuroscience*, *34*(46), 15208–15222. https://doi.org/10.1523/JNEUROSCI.1747-14.2014

Evangelista, E., Bénar, C., Bonini, F., Carron, R., Colombet, B., Régis, J., & Bartolomei, F. (2015). Does the Thalamo-Cortical Synchrony Play a Role in Seizure Termination? *Frontiers in Neurology*, *6*. https://doi.org/10.3389/fneur.2015.00192

Feng, Z., & Durand, D. M. (2003). Low-Calcium Epileptiform Activity in the Hippocampus In Vivo. *Journal of Neurophysiology*, *90*(4), 2253–2260. https://doi.org/10.1152/jn.00241.2003

Fisher, R. S., Pedley, T. A., Moody, W. J., & Prince, D. A. (1976). The Role of Extracellular Potassium in Hippocampal Epilepsy. *Archives of Neurology*, *33*(2), 76–83. https://doi.org/10.1001/archneur.1976.00500020004002

Fisher, Robert S., & Schachter, S. C. (2000). The Postictal State: A Neglected Entity in the

Management of Epilepsy. *Epilepsy and Behavior*, *1*(1), 52–59. https://doi.org/10.1006/ebeh.2000.0023

Franaszczuk, P. J., Bergey, G. K., Durka, P. J., & Eisenberg, H. M. (1998). Time-frequency analysis using the matching pursuit algorithm applied to seizures originating from the mesial temporal lobe. *Electroencephalography and Clinical Neurophysiology*, *106*(6), 513–521. https://doi.org/10.1016/S0013-4694(98)00024-8

Fransen, E., Alonso, A. A., & Hasselmo, M. E. (2002). Simulations of the role of the muscarinic-activated calcium-sensitive nonspecific cation current INCM in entorhinal neuronal activity during delayed matching tasks. *Journal of Neuroscience*, *22*(3), 1081–1097. https://doi.org/10.1523/jneurosci.22-03-01081.2002

Fröhlich, F., Bazhenov, M., Timofeev, I., Steriade, M., & Sejnowski, T. J. (2006). Slow state transitions of sustained neural oscillations by activity-dependent modulation of intrinsic excitability. *Journal of Neuroscience*, *26*(23), 6153–6162. https://doi.org/10.1523/JNEUROSCI.5509-05.2006

Fujiwara-Tsukamoto, Y., Isomura, Y., Imanishi, M., Fukai, T., & Takada, M. (2007). Distinct types of ionic modulation of GABA actions in pyramidal cells and interneurons during electrical induction of hippocampal seizure-like network activity. *European Journal of Neuroscience*, *25*(9), 2713–2725. https://doi.org/10.1111/j.1460-9568.2007.05543.x

Futamachi, K. J., Mutani, R., & Prince, D. A. (1974). Potassium activity in rabbit cortex. *Brain Research*, *75*(1), 5–25. https://doi.org/10.1016/0006-8993(74)90767-7

Gentiletti, D., Suffczynski, P., Gnatkovsky, V., & De Curtis, M. (2017). Changes of Ionic Concentrations during Seizure Transitions-A Modeling Study. *International Journal of Neural Systems*, *27*(4), 1–16. https://doi.org/10.1142/S0129065717500046

Gnatkovsky, V., Librizzi, L., Trombin, F., & De Curtis, M. (2008). Fast activity at seizure onset is mediated by inhibitory circuits in the entorhinal cortex in vitro. *Annals of Neurology*, *64*(6), 674–686. https://doi.org/10.1002/ana.21519

Golomb, D., Yue, C., & Yaari, Y. (2006). Contribution of Persistent Na + Current and M-Type K + Current to Somatic Bursting in CA1 Pyramidal Cells: Combined Experimental and

Modeling Study. *Journal of Neurophysiology*, *96*(4), 1912–1926. https://doi.org/10.1152/jn.00205.2006

González, O. C., Shiri, Z., Krishnan, G. P., Myers, T. L., Williams, S., Avoli, M., & Bazhenov, M. (2018). Role of KCC2-dependent potassium efflux in 4-Aminopyridine-induced Epileptiform synchronization. *Neurobiology of Disease*, *109*(August 2017), 137–147. https://doi.org/10.1016/j.nbd.2017.10.011

Grasse, D. W., Karunakaran, S., & Moxon, K. A. (2013). Neuronal synchrony and the transition to spontaneous seizures. *Experimental Neurology*, *248*, 72–84. https://doi.org/10.1016/j.expneurol.2013.05.004

Grigorovsky, V., Jacobs, D., Breton, V. L., Tufa, U., Lucasius, C., del Campo, J. M., Chinvarun, Y., Carlen, P. L., Wennberg, R., & Bardakjian, B. L. (2020). Delta-gamma phase-amplitude coupling as a biomarker of postictal generalized EEG suppression. *Brain Communications*, *2*(2). https://doi.org/10.1093/braincomms/fcaa182

Haas, H. L., & Jefferys, J. G. (1984). Low-calcium field burst discharges of CA1 pyramidal neurones in rat hippocampal slices. *The Journal of Physiology*, *354*(1), 185–201. https://doi.org/10.1113/jphysiol.1984.sp015371

Hamidi, S., & Avoli, M. (2015). KCC2 function modulates in vitro ictogenesis. *Neurobiology of Disease*, *79*, 51–58. https://doi.org/10.1016/j.nbd.2015.04.006

Heinemann, U., Lux, H. D., & Gutnick, M. J. (1977). Extracellular free calcium and potassium during paroxysmal activity in the cerebral cortex of the cat. *Experimental Brain Research*, *27*(3–4), 237–243. https://doi.org/10.1007/BF00235500

Heinemann, Uwe, & Lux, H. D. (1975). Undershoots following stimulus-induced rises of extracellular potassium concentration in cerebral cortex of cat. *Brain Research*, *93*(1), 63–76. https://doi.org/10.1016/0006-8993(75)90286-3

Ho, Y. E. C., & Truccolo, W. (2016). Interaction between synaptic inhibition and glial-potassium dynamics leads to diverse seizure transition modes in biophysical models of human focal seizures. *Journal of Computational Neuroscience*, *41*(2), 225–244. https://doi.org/10.1007/s10827-016-0615-7

Hübel, N., & Ullah, G. (2016). Anions Govern Cell Volume: A Case Study of Relative Astrocytic and Neuronal Swelling in Spreading Depolarization. *PLOS ONE*, *11*(3), e0147060. https://doi.org/10.1371/journal.pone.0147060

Igelström, K. M. (2013). Is Slack an Intrinsic Seizure Terminator? *The Neuroscientist*, *19*(3), 248–254. https://doi.org/10.1177/1073858412446311

Jedlicka, P., Deller, T., Gutkin, B. S., & Backus, K. H. (2010). Activity-dependent intracellular chloride accumulation and diffusion controls GABAA receptor-mediated synaptic transmission. *Hippocampus*, n/a-n/a. https://doi.org/10.1002/hipo.20804

Jefferys, J. G. (1995). Nonsynaptic modulation of neuronal activity in the brain: electric currents and extracellular ions. *Physiological Reviews*, *75*(4), 689–723. https://doi.org/10.1152/physrev.1995.75.4.689

Jefferys, J. G. R., & Haas, H. L. (1982). Synchronized bursting of CA1 hippocampal pyramidal cells in the absence of synaptic transmission. *Nature*, *300*(5891), 448–450. https://doi.org/10.1038/300448a0

Jefferys, J., Jiruska, P., de Curtis, M., & Avoli, M. (2012). Limbic Network Synchronization and Temporal Lobe Epilepsy. In J. Noebels, M. Avoli, M. Rogawski, R. Olsen, & A. Delgado-Escueta (Eds.), *Jasper's Basic Mechanisms of the Epilepsies*. Bethesda (MD): National Center for Biotechnology Information (US). http://www.ncbi.nlm.nih.gov/pubmed/22787650

Jensen, M. S., & Yaari, Y. (1997). Role of intrinsic burst firing, potassium accumulation, and electrical coupling in the elevated potassium model of hippocampal epilepsy. *Journal of Neurophysiology*, *77*(3), 1224–1233. https://doi.org/10.1152/jn.1997.77.3.1224

Jirsa, V. K., Stacey, W. C., Quilichini, P. P., Ivanov, A. I., & Bernard, C. (2014). On the nature of seizure dynamics. *Brain*, *137*(8), 2210–2230. https://doi.org/10.1093/brain/awu133

Kager, H., Wadman, W. J., & Somjen, G. G. (2000). Simulated Seizures and Spreading Depression in a Neuron Model Incorporating Interstitial Space and Ion Concentrations. *Journal of Neurophysiology*, *84*(1), 495–512. https://doi.org/10.1152/jn.2000.84.1.495

Kager, H., Wadman, W. J., & Somjen, G. G. (2002). Conditions for the triggering of spreading depression studied with computer simulations. *Journal of Neurophysiology*, *88*(5), 2700–2712. https://doi.org/10.1152/jn.00237.2002

Kaila, K., Lamsa, K., Smirnov, S., Taira, T., & Voipio, J. (1997). Long-lasting GABA-mediated depolarization evoked by high-frequency stimulation in pyramidal neurons of rat hippocampal slice is attributable to a network-driven, bicarbonate-dependent K+ transient. *Journal of Neuroscience*, *17*(20), 7662–7672. https://doi.org/10.1523/jneurosci.17-20-07662.1997

Kaila, K., Price, T. J., Payne, J. A., Puskarjov, M., & Voipio, J. (2014). Cation-chloride cotransporters in neuronal development, plasticity and disease. *Nature Reviews Neuroscience*, *15*(10), 637–654. https://doi.org/10.1038/nrn3819

Kalitzin, S. N., Bauer, P. R., Lamberts, R. J., Velis, D. N., Thijs, R. D., & Da Silva, F. H. L. (2016). Automated Video Detection of Epileptic Convulsion Slowing as a Precursor for Post-Seizure Neuronal Collapse. *International Journal of Neural Systems*, *26*(8), 100–104. https://doi.org/10.1142/S0129065716500271

Krishnan, G. P., & Bazhenov, M. (2011). Ionic dynamics mediate spontaneous termination of seizures and postictal depression state. *Journal of Neuroscience*, *31*(24), 8870–8882. https://doi.org/10.1523/JNEUROSCI.6200-10.2011

Krishnan, G. P., Filatov, G., Shilnikov, A., & Bazhenov, M. (2015). Electrogenic properties of the Na+/K+ ATPase control transitions between normal and pathological brain states. *Journal of Neurophysiology*, *113*(9), 3356–3374. https://doi.org/10.1152/jn.00460.2014

Lado, F. A., & Moshé, S. L. (2008). How do seizures stop? *Epilepsia*, *49*(10), 1651–1664. https://doi.org/10.1111/j.1528-1167.2008.01669.x

Lagarde, S., Buzori, S., Trebuchon, A., Carron, R., Scavarda, D., Milh, M., McGonigal, A., & Bartolomei, F. (2019). The repertoire of seizure onset patterns in human focal epilepsies: Determinants and prognostic values. *Epilepsia*, *60*(1), 85–95. https://doi.org/10.1111/epi.14604

Lévesque, M., Herrington, R., Hamidi, S., & Avoli, M. (2016). Interneurons spark seizure-like

activity in the entorhinal cortex. *Neurobiology of Disease*, *87*, 91–101. https://doi.org/10.1016/j.nbd.2015.12.011

Lian, J., Bikson, M., Shuai, J., & Durand, D. M. (2001). Propagation of non-synaptic epileptiform activity across a lesion in rat hippocampal slices. *Journal of Physiology*, *537*(1), 191–199. https://doi.org/10.1111/j.1469-7793.2001.0191k.x

Lillis, K. P., Kramer, M. A., Mertz, J., Staley, K. J., & White, J. A. (2012). Pyramidal cells accumulate chloride at seizure onset. *Neurobiology of Disease*, *47*(3), 358–366. https://doi.org/10.1016/j.nbd.2012.05.016

Lindén, H., Hagen, E., Łeski, S., Norheim, E. S., Pettersen, K. H., & Einevoll, G. T. (2014). LFPy: A tool for biophysical simulation of extracellular potentials generated by detailed model neurons. *Frontiers in Neuroinformatics*, *7*(JAN), 1–15. https://doi.org/10.3389/fninf.2013.00041

Liou, J., Smith, E. H., Bateman, L. M., Bruce, S. L., McKhann, G. M., Goodman, R. R., Emerson, R. G., Schevon, C. A., & Abbott, L. (2020). A model for focal seizure onset, propagation, evolution, and progression. *ELife*, *9*. https://doi.org/10.7554/eLife.50927

Lopantsev, V., & Avoli, M. (1998). Participation of GABA(A)-mediated inhibition in ictallike discharges in the rat entorhinal cortex. *Journal of Neurophysiology*, *79*(1), 352–360. https://doi.org/10.1152/jn.1998.79.1.352

Magistretti, J., & Alonso, A. (1999). Biophysical Properties and Slow Voltage-Dependent Inactivation of a Sustained Sodium Current in Entorhinal Cortex Layer-II Principal Neurons. *Journal of General Physiology*, *114*(4), 491–509. https://doi.org/10.1085/jgp.114.4.491

Magloire, V., Cornford, J., Lieb, A., Kullmann, D. M., & Pavlov, I. (2019). KCC2 overexpression prevents the paradoxical seizure-promoting action of somatic inhibition. *Nature Communications*, *10*(1), 1–13. https://doi.org/10.1038/s41467-019-08933-4

Magloire, V., Mercier, M. S., Kullmann, D. M., & Pavlov, I. (2019). GABAergic Interneurons in Seizures: Investigating Causality With Optogenetics. *The Neuroscientist*, *25*(4), 344–358. https://doi.org/10.1177/1073858418805002

Martinet, L.-E., Fiddyment, G., Madsen, J. R., Eskandar, E. N., Truccolo, W., Eden, U. T., Cash, S. S., & Kramer, M. A. (2017). Human seizures couple across spatial scales through travelling wave dynamics. *Nature Communications*, *8*(1), 14896. https://doi.org/10.1038/ncomms14896

McBain, C., Traynelis, S., & Dingledine, R. (1990). Regional variation of extracellular space in the hippocampus. *Science*, *249*(4969), 674–677. https://doi.org/10.1126/science.2382142

Miles, R., Blaesse, P., Huberfeld, G., Wittner, L., & Kaila, K. (2012). Chloride homeostasis and GABA signaling in temporal lobe epilepsy. In D.-E. A. Noebels JL, Avoli M, Rogawski MA, Olsen RW (Ed.), *Jasper's Basic Mechanisms of the Epilepsies*. National Center for Biotechnology Information (US). http://www.ncbi.nlm.nih.gov/pubmed/22787654

Miri, M. L., Vinck, M., Pant, R., & Cardin, J. A. (2018). Altered hippocampal interneuron activity precedes ictal onset. *ELife*, *7*. https://doi.org/10.7554/eLife.40750

Moore, Y. E., Deeb, T. Z., Chadchankar, H., Brandon, N. J., & Moss, S. J. (2018). Potentiating KCC2 activity is sufficient to limit the onset and severity of seizures. *Proceedings of the National Academy of Sciences of the United States of America*, *115*(40), 10166–10171. https://doi.org/10.1073/pnas.1810134115

Nunez, P. L., & Srinivasan, R. (2006). *Electric Fields of the Brain*. Oxford University Press. https://doi.org/10.1093/acprof:oso/9780195050387.001.0001

Payne, D. E., Karoly, P. J., Freestone, D. R., Boston, R., D'Souza, W., Nurse, E., Kuhlmann, L., Cook, M. J., & Grayden, D. B. (2018). Postictal suppression and seizure durations: A patient-specific, long-term iEEG analysis. *Epilepsia*, *59*(5), 1027–1036. https://doi.org/10.1111/epi.14065

Payne, J. A. (1997). Functional characterization of the neuronal-specific K-Cl cotransporter: Implications for [K+](o) regulation. *American Journal of Physiology - Cell Physiology*, *273*(5 42-5). https://doi.org/10.1152/ajpcell.1997.273.5.c1516

Payne, J. A., Rivera, C., Voipio, J., & Kaila, K. (2003). Cation-chloride co-transporters in

neuronal communication, development and trauma. *Trends in Neurosciences*, *26*(4), 199–206. https://doi.org/10.1016/S0166-2236(03)00068-7

Perucca, P., Dubeau, F., & Gotman, J. (2014). Intracranial electroencephalographic seizure-onset patterns: effect of underlying pathology. *Brain*, *137*(1), 183–196. https://doi.org/10.1093/brain/awt299

Pottkämper, J. C. M., Hofmeijer, J., van Waarde, J. A., & van Putten, M. J. A. M. (2020). The postictal state — What do we know? *Epilepsia*, *61*(6), 1045–1061. https://doi.org/10.1111/epi.16519

Proix, T., Jirsa, V. K., Bartolomei, F., Guye, M., & Truccolo, W. (2018). Predicting the spatiotemporal diversity of seizure propagation and termination in human focal epilepsy. *Nature Communications*, *9*(1), 1088. https://doi.org/10.1038/s41467-018-02973-y

Pumain, R., Menini, C., Heinemann, U., Louvel, J., & Silva-Barrat, C. (1985). Chemical synaptic transmission is not necessary for epileptic seizures to persist in the baboon Papio papio. *Experimental Neurology*, *89*(1), 250–258. https://doi.org/10.1016/0014-4886(85)90280-8

Raimondo, J. (2013). A genetically-encoded chloride and pH sensor for dissociating ion dynamics in the nervous system. *Frontiers in Cellular Neuroscience*, *7*. https://doi.org/10.3389/fncel.2013.00202

Raimondo, J. V., Burman, R. J., Katz, A. A., & Akerman, C. J. (2015). Ion dynamics during seizures. *Frontiers in Cellular Neuroscience*, *9*, 1–14. https://doi.org/10.3389/fncel.2015.00419

Saggio, M. L., Crisp, D., Scott, J. M., Karoly, P., Kuhlmann, L., Nakatani, M., Murai, T., Dümpelmann, M., Schulze-Bonhage, A., Ikeda, A., Cook, M., Gliske, S. V, Lin, J., Bernard, C., Jirsa, V., & Stacey, W. C. (2020). A taxonomy of seizure dynamotypes. *ELife*, *9*. https://doi.org/10.7554/eLife.55632

Schiff, S. J., Colella, D., Jacyna, G. M., Hughes, E., Creekmore, J. W., Marshall, A., Bozek-Kuzmicki, M., Benke, G., Gaillard, W. D., Conry, J., & Weinstein, S. R. (2000). Brain chirps: spectrographic signatures of epileptic seizures. *Clinical Neurophysiology*, *111*(6),

953–958. https://doi.org/10.1016/S1388-2457(00)00259-5

Schindler, K., Leung, H., Elger, C. E., & Lehnertz, K. (2007). Assessing seizure dynamics by analysing the correlation structure of multichannel intracranial EEG. *Brain*, *130*(1), 65–77. https://doi.org/10.1093/brain/awl304

Shivacharan, R. S., Chiang, C.-C., Zhang, M., Gonzalez-Reyes, L. E., & Durand, D. M. (2019). Self-propagating, non-synaptic epileptiform activity recruits neurons by endogenous electric fields. *Experimental Neurology*, *317*, 119–128. https://doi.org/10.1016/j.expneurol.2019.02.005

Somjen, G. G., Kager, H., & Wadman, W. J. (2008). Computer simulations of neuron-glia interactions mediated by ion flux. *Journal of Computational Neuroscience*, *25*(2), 349–365. https://doi.org/10.1007/s10827-008-0083-9

Spencer, S. S., Guimaraes, P., Katz, A., Kim, J., & Spencer, D. (1992). Morphological Patterns of Seizures Recorded Intracranially. *Epilepsia*, *33*(3), 537–545. https://doi.org/10.1111/j.1528-1157.1992.tb01706.x

Staley, K. J., & Proctor, W. R. (1999). Modulation of mammalian dendritic GABA A receptor function by the kinetics of Cl − and HCO 3 − transport. *The Journal of Physiology*, *519*(3), 693–712. https://doi.org/10.1111/j.1469-7793.1999.0693n.x

Staley, K. J., Soldo, B. L., & Proctor, W. R. (1995). Ionic Mechanisms of Neuronal Excitation by Inhibitory GABA A Receptors. *Science*, *269*(5226), 977–981. https://doi.org/10.1126/science.7638623

Suffczynski, P., Gentiletti, D., Gnatkovsky, V., & de Curtis, M. (2017). Extracellular Potassium and Focal Seizures—Insight from In Silico Study. In P. Érdi, B. Sen Bhattacharya, & A. Cochran (Eds.), *Computational Neurology and Psychiatry. Springer Series in Bio-/Neuroinformatics* (pp. 49–72). Springer, Cham. https://doi.org/10.1007/978-3-319-49959-8_3

Sulis Sato, S., Artoni, P., Landi, S., Cozzolino, O., Parra, R., Pracucci, E., Trovato, F., Szczurkowska, J., Luin, S., Arosio, D., Beltram, F., Cancedda, L., Kaila, K., & Ratto, G. M. (2017). Simultaneous two-photon imaging of intracellular chloride concentration and

pH in mouse pyramidal neurons in vivo. *Proceedings of the National Academy of Sciences*, *114*(41), E8770–E8779. https://doi.org/10.1073/pnas.1702861114

Theparambil, S. M., Hosford, P. S., Ruminot, I., Kopach, O., Reynolds, J. R., Sandoval, P. Y., Rusakov, D. A., Barros, L. F., & Gourine, A. V. (2020). Astrocytes regulate brain extracellular pH via a neuronal activity-dependent bicarbonate shuttle. *Nature Communications*, *11*(1), 5073. https://doi.org/10.1038/s41467-020-18756-3

Thompson, S. M., & Gahwiler, B. H. (1989). Activity-dependent disinhibition. II. Effects of extracellular potassium, furosemide, and membrane potential on ECl- in hippocampal CA3 neurons. *Journal of Neurophysiology*, *61*(3), 512–523. https://doi.org/10.1152/jn.1989.61.3.512

Timofeev, I., & Steriade, M. (2004). Neocortical seizures: initiation, development and cessation. *Neuroscience*, *123*(2), 299–336. https://doi.org/10.1016/j.neuroscience.2003.08.051

Toyoda, I., Fujita, S., Thamattoor, A. K., & Buckmaster, P. S. (2015). Unit Activity of Hippocampal Interneurons before Spontaneous Seizures in an Animal Model of Temporal Lobe Epilepsy. *Journal of Neuroscience*, *35*(16), 6600–6618. https://doi.org/10.1523/JNEUROSCI.4786-14.2015

Traub, R. D., Buhl, E. H., Gloveli, T., & Whittington, M. A. (2003). Fast Rhythmic Bursting Can Be Induced in Layer 2/3 Cortical Neurons by Enhancing Persistent Na + Conductance or by Blocking BK Channels. *Journal of Neurophysiology*, *89*(2), 909–921. https://doi.org/10.1152/jn.00573.2002

Traynelis, S. F., & Dingledine, R. (1988). Potassium-induced spontaneous electrographic seizures in the rat hippocampal slice. *Journal of Neurophysiology*, *59*(1), 259–276. https://doi.org/10.1152/jn.1988.59.1.259

Truccolo, W., Donoghue, J. A., Hochberg, L. R., Eskandar, E. N., Madsen, J. R., Anderson, W. S., Brown, E. N., Halgren, E., & Cash, S. S. (2011). Single-neuron dynamics in human focal epilepsy. *Nature Neuroscience*, *14*(5), 635–643. https://doi.org/10.1038/nn.2782

Uva, L., Breschi, G. L., Gnatkovsky, V., Taverna, S., & de Curtis, M. (2015). Synchronous

inhibitory potentials precede seizure-like events in acute models of focal limbic seizures. *Journal of Neuroscience*, *35*(7), 3048–3055. https://doi.org/10.1523/JNEUROSCI.3692-14.2015

Uva, L., & de Curtis, M. (2020). Activity- and pH-dependent adenosine shifts at the end of a focal seizure in the entorhinal cortex. *Epilepsy Research*, *165*, 106401. https://doi.org/10.1016/j.eplepsyres.2020.106401

Velascol, A. L., Wilson, C. L., Babb, T. L., & Engel Jr, J. (2000). Functional and Anatomic Correlates of Two Frequently Observed Temporal Lobe Seizure-Onset Patterns. *Neural Plasticity*, *7*(1–2), 49–63. https://doi.org/10.1155/NP.2000.49

Viitanen, T., Ruusuvuori, E., Kaila, K., & Voipio, J. (2010). The K+-Cl- cotransporter KCC2 promotes GABAergic excitation in the mature rat hippocampus. *Journal of Physiology*, *588*(9), 1527–1540. https://doi.org/10.1113/jphysiol.2009.181826

Wei, Y., Ullah, G., Ingram, J., & Schiff, S. J. (2014). Oxygen and seizure dynamics: II. Computational modeling. *Journal of Neurophysiology*, *112*(2), 213–223. https://doi.org/10.1152/jn.00541.2013

Wei, Y., Ullah, G., & Schiff, S. J. (2014). Unification of neuronal spikes, seizures, and spreading depression. *Journal of Neuroscience*, *34*(35), 11733–11743. https://doi.org/10.1523/JNEUROSCI.0516-14.2014

Wen, B., Qian, H., Feng, J., Ge, R.-J., Xu, X., Cui, Z.-Q., Zhu, R.-Y., Pan, L.-S., Lin, Z.-P., & Wang, J.-H. (2015). A Portion of Inhibitory Neurons in Human Temporal Lobe Epilepsy are Functionally Upregulated: An Endogenous Mechanism for Seizure Termination. *CNS Neuroscience & Therapeutics*, *21*(2), 204–214. https://doi.org/10.1111/cns.12336

Yaari, Y., Konnerth, A., & Heinemann, U. (1983). Spontaneous epileptiform activity of ca1 hippocampal neurons in low extracellular calcium solutions. *Experimental Brain Research*, *51*(1). https://doi.org/10.1007/BF00236813

Yekhlef, L., Breschi, G. L., Lagostena, L., Russo, G., & Taverna, S. (2015). Selective activation of parvalbumin- or somatostatin-expressing interneurons triggers epileptic seizurelike activity in mouse medial entorhinal cortex. *Journal of Neurophysiology*,

113(5), 1616–1630. https://doi.org/10.1152/jn.00841.2014

Ziburkus, J., Cressman, J. R., Barreto, E., & Schiff, S. J. (2006). Interneuron and pyramidal cell interplay during in vitro seizure-like events. *Journal of Neurophysiology*, *95*(6), 3948–3954. https://doi.org/10.1152/jn.01378.2005

Ziemann, A. E., Schnizler, M. K., Albert, G. W., Severson, M. A., Howard III, M. A., Welsh, M. J., & Wemmie, J. A. (2008). Seizure termination by acidosis depends on ASIC1a. *Nature Neuroscience*, *11*(7), 816–822. https://doi.org/10.1038/nn.2132

Zubler, F., Steimer, A., Gast, H., & Schindler, K. A. (2014). Seizure Termination. In *International Review of Neurobiology* (pp. 187–207). Academic Press Inc. https://doi.org/10.1016/B978-0-12-418693-4.00008-X

Appendix I

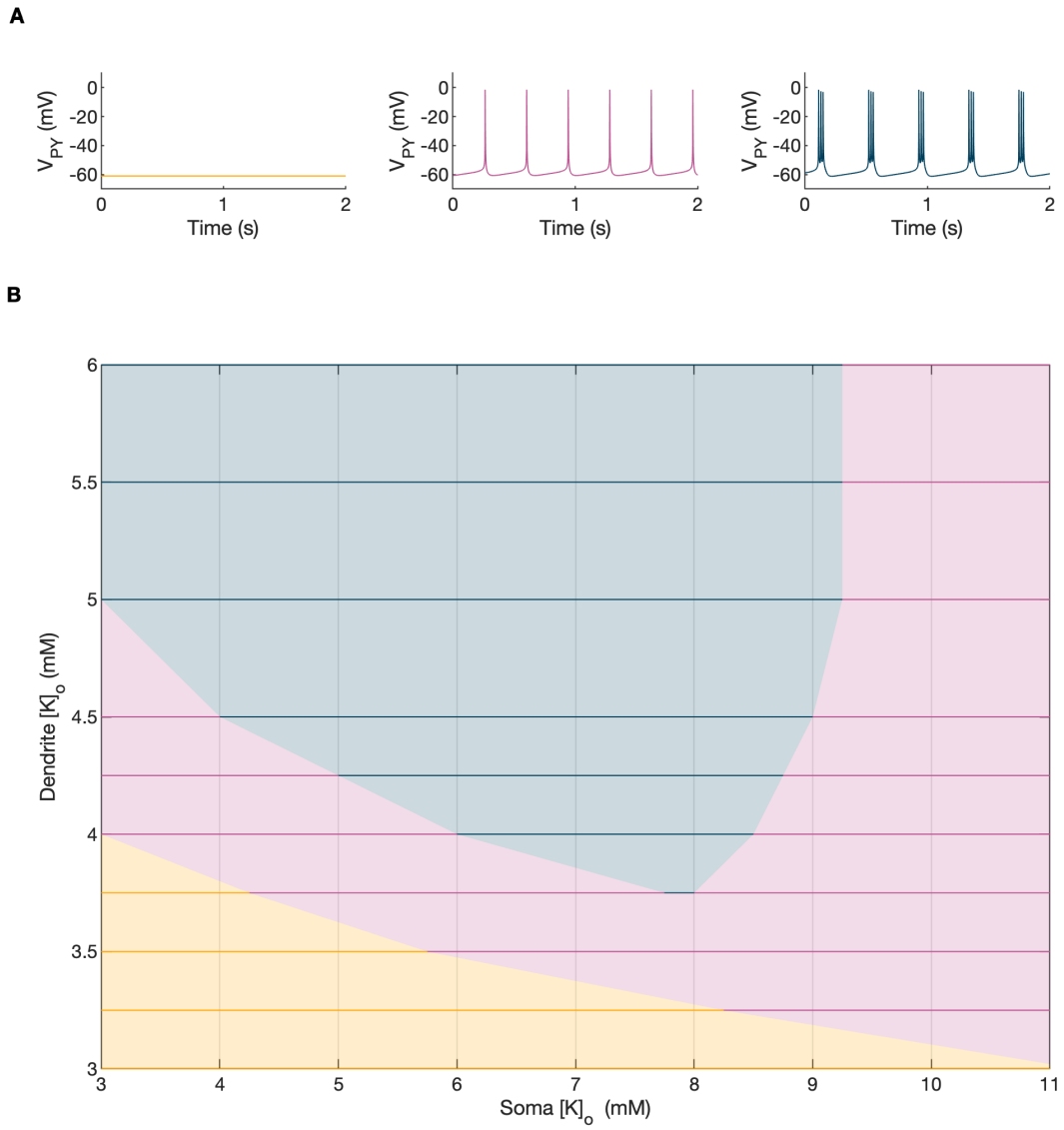

Appendix I - figure 1. A bifurcation diagram of a single PY cell. The 2D bifurcation diagram demonstrates the behavior of a single PY cell as a function of extracellular potassium concentration in the dendritic ($[K^+]_{o,dend}$) and somatic compartments ($[K^+]_{o,soma}$) used as control parameters. Concentrations of all other ions were fixed at their reference values (except chloride: $[Cl^-]_{i,soma}$, $[Cl^-]_{i,dend}$ equal to 7 mM), all ion accumulation mechanisms were blocked and all synaptic connections were removed. **(A)** The three graphs show the PY cell activity traces for different values of the control parameters: resting (yellow, $[K^+]_{o,soma}$ = 3.5 mM, $[K^+]_{o,dend}$ = 3.5 mM), tonic firing (violet, $[K^+]_{o,soma}$ = 4.5 mM, $[K^+]_{o,dend}$ = 4 mM) and bursting (dark blue,

$[K^+]_{o,soma}$ = 6.5 mM, $[K^+]_{o,dend}$ = 4 mM). In each panel, 2 seconds of activity is shown. **(B)** The colors of the 2D diagram correspond to the types of activity shown above in **(A)**. For low $[K^+]_{o,dend}$ and $[K^+]_{o,soma}$ the cell was at rest. A moderate increase in either $[K^+]_{o,dend}$ or $[K^+]_{o,soma}$, or both, led to tonic firing. Subsequent increases in these parameters led to bursting.

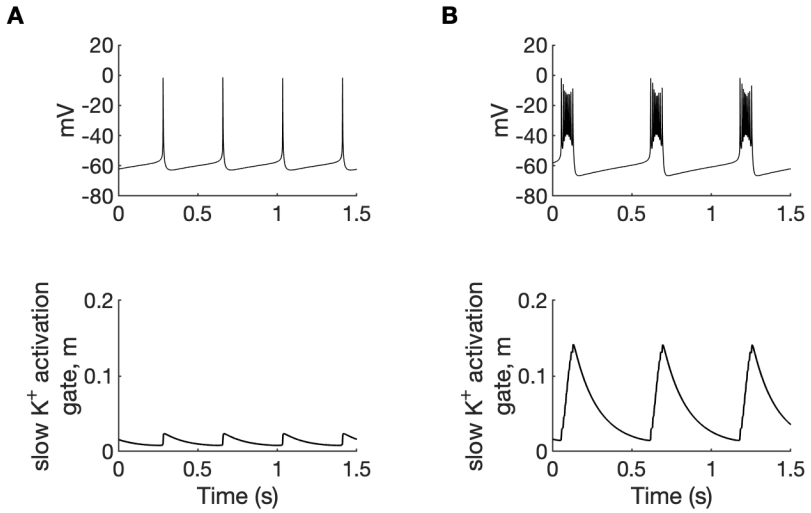

Appendix I - figure 2. A comparison of tonic firing (A) and bursting (B) of a PY cell. In each column, the membrane potential of a cell (top) and the activation gate of I_{KM} (bottom) is shown. During tonic firing, the activation gate of the M-type potassium current was closed. The prolonged depolarization of the cell during bursting led to the opening of the activation gate *m* and activation of the I_{KM} current, which eventually terminated the burst. The simulation was performed using an isolated PY cell model with the concentrations of all ions fixed at their reference values, except $[Cl^-]_{i,soma}$= 7, $[Cl^-]_{i,dend}$ = 7 mM and **(A)**: $[K^+]_{o,soma}$ = 3.5 mM, $[K^+]_{o,dend}$ = 4.5 mM, **(B)**: $[K^+]_{o,soma}$ = 5.25 mM and $[K^+]_{o,dend}$ = 4.5 mM.

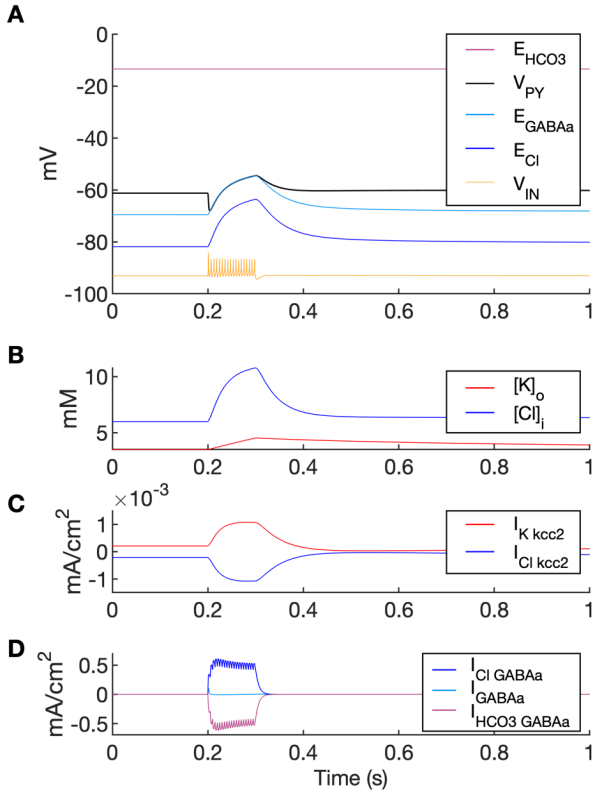

1381

1382 **Appendix I - figure 3. A simulation of biphasic GABAa response.** In this simulation size of
1383 both PY compartments was scaled down by factor 10, to represent small dendritic compartments.
1384 Single GABAa synapse was located in a segment having diameter 1.5 um and length 2 um (i.e.,
1385 having volume 1000 times smaller and GABAa conductance density 100 times larger than soma
1386 in the original model). **(A)** High frequency IN firing (shown schematically by V_{IN}, yellow; not
1387 to scale) was induced by IN current stimulation of 100 ms duration. GABAa receptor-mediated
1388 postsynaptic potential response consisted of the initial hyperpolarization followed by a long-
1389 lasting depolarization (V_{PY}, black). Chloride accumulation (**(B)**, blue) was mediated by large Cl^-
1390 influx via GABAa receptor as compared to Cl^- extrusion via KCC2 (**(C)** vs. **(D)**). Accordingly,
1391 the biphasic potential resulted from positive shift in E_{Cl} (**(A)**, blue) and relatively high E_{HCO3}
1392 (**(A)**, violet) leading to depolarizing shift in E_{GABAa} (**(A),** light blue). During GABAa receptor
1393 activation V_{PY} was clamped to E_{GABAa} due to large GABAa conductance density.

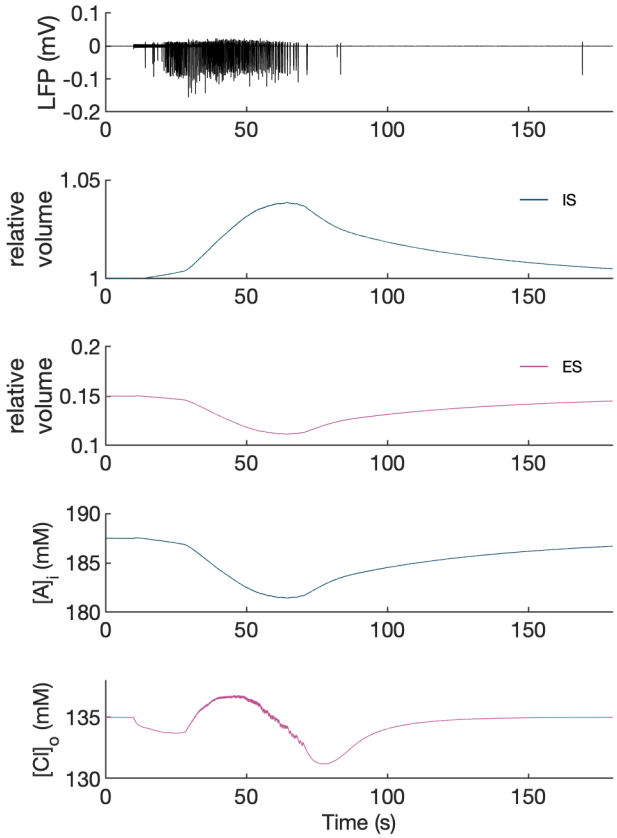

1394

1395 **Appendix I - figure 4. Volume changes during an SLE in the model.** The panels show from
1396 top to bottom: LFP, relative volume changes and representative changes in intracellular A^- ion
1397 and extracellular Cl^- concentration in the PY somatic compartment during an SLE. $[A^-]_i$ was
1398 affected only by volume changes while $[Cl^-]_o$ was additionally affected by inward chloride leak
1399 and GABAa currents, KCC2 and Cl^- diffusion to the bath. It can be seen that an increase in
1400 intracellular space (IS) volume (second panel, dark blue) is exactly mirrored by a decrease in $[A^-$
1401 $]_i$. A decrease in extracellular space (ES) volume (third panel, violet) gives rise to an increase in
1402 $[Cl^-]_o$ above baseline despite Cl^- influx into the cells, in agreement with the experimental data
1403 (Dietzel et al., 1982).